

pubs.acs.org/acscatalysis Research Article

# Bismuth-Modulated Surface Structural Evolution of Pd<sub>3</sub>Bi Intermetallic Alloy Catalysts for Selective Propane Dehydrogenation and Acetylene Semihydrogenation

Wenqing Zhang,<sup>#</sup> Xiaoben Zhang,<sup>#</sup> Jianyang Wang, Arnab Ghosh, Jie Zhu, Nicole J. LiBretto, Guanghui Zhang,<sup>\*</sup> Abhaya K. Datye, Wei Liu,<sup>\*</sup> and Jeffrey T. Miller<sup>\*</sup>



Cite This: ACS Catal. 2022, 12, 10531-10545



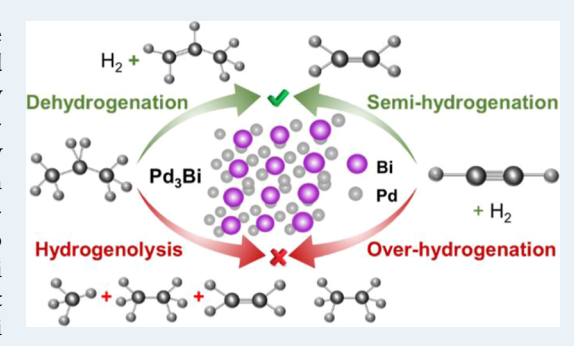
**ACCESS** I

III Metrics & More

Article Recommendations

s Supporting Information

**ABSTRACT:** Atomic regulation of metal catalysts, especially of the active surface, is key to optimizing the catalytic performance. In this work, we tuned surface Pd coordination by varying bismuth loadings in the Pd—Bi alloy system, facilitating different catalytic performances for propane dehydrogenation (PDH) and acetylene semihydrogenation model reactions. *In situ X-ray* absorption spectroscopy, atom-resolved scanning transmission electron microscopy combined with elemental distribution analysis, infrared spectroscopy, and *in situ X-ray* photoelectron spectroscopy were employed to characterize the evolution of the surface and bulk structures in Pd—Bi catalysts with changing Bi composition. At low Bi loading, the catalyst nanoparticle (NP) surface was partially transformed into the Pd—Bi intermetallic compound (IMC). The partially alloyed surface has improved



catalytic performance compared with Pd NPs. At slightly higher Bi loading, a Pd core—Pd<sub>3</sub>Bi shell structure was formed, which displayed significantly improved selectivity rate and stability. In the Pd<sub>3</sub>Bi IMC surface structure, the adjacent Pd atoms are sufficiently far apart to give catalytically isolated active sites, which significantly enhance the selectivity (>95%) to propylene in PDH and give a higher ethylene selectivity (80%) for acetylene semihydrogenation compared with Pd NPs. At higher Bi loading, a full Pd<sub>3</sub>Bi is formed; however, at even higher loading, an overcoating of excess BiO<sub>x</sub> leads to a loss in activity. This work demonstrates that in intermetallic alloy catalysts, the surface and bulk structures of the NPs are different with different promoter metal loadings. Importantly, the catalyst performance is not only determined by the alloy structure but also can be significantly affected by the properties of the noncatalytic oxide promoter.

**KEYWORDS:** EXAFS NP surface determination,  $Pd_3Bi$  propane dehydrogenation,  $Pd_3Bi$  acetylene semihydrogenation, evolution of intermetallic alloy NP formation, effect of noncatalytic oxide on rate

## 1. INTRODUCTION

The catalytic impact of nanostructural engineering typically originates from surface modification at the atomic scale. Selectivity, the ability to drive a reaction in a specific direction in preference to others, is a crucial attribute of catalysts. More selective catalytic processes require less reactants and produce fewer byproducts with less subsequent separation.<sup>2–5</sup> From the economic and environmental perspectives, the development of selective catalysts is vital and has sparked highly interdisciplinary research efforts aimed at engineering the atomic structure on the catalytic surfaces and understanding the associated electronic and geometric properties of surface atoms. Prototypical examples include propane dehydrogenation (PDH) and acetylene semihydrogenation reactions. Specifically, PDH is an endothermic reaction and requires high temperature (773-973 K), where hydrogenolysis, a structuresensitive reaction, also occurs on Pd ensembles forming methane, ethane, and ethylene, leading to low propylene

selectivity,<sup>7–11</sup> while acetylene semihydrogenation proceeds under milder reaction conditions (323–573 K), selectively removes trace amounts of acetylene impurities in the ethylene feed is a crucial step for the production of polymer-grade ethylene for polyethylene production, especially in the frontend process. <sup>12–16</sup> Palladium (Pd) is highly active for these two catalytic processes but exhibits low selectivity toward the desired products. <sup>9,17–20</sup> Therefore, developing fundamental understandings on how to improve the selectivity will lead to effective catalysts for these and other catalytic reactions.

Received: March 9, 2022 Revised: July 8, 2022 Published: August 11, 2022





The incorporation of a second metal to form intermetallic alloys or intermetallic compounds (IMCs) has been used to reduce the surface ensemble size to enhance the olefin selectivity in PDH and acetylene semihydrogenation. For example, a variety of intermetallic Pd catalysts, Pd-Fe, Pd-Mn, Pd-Cu, Pd-In, Pd-Ga, Pd-Ag, Pd-Au, and Pd-Zn, have shown substantially enhanced olefin selectivity for PDH and acetylene semihydrogenation compared with Pd nanoparticles (NPs). 9,15,16,20-25 Among these different types of bimetallic catalysts, the changes in the structure with different compositions lead to differences in catalytic performance. For some compositions, a random distribution of metallic atoms or in other words solid solution is formed.<sup>26</sup> For other bimetallic catalysts, IMCs are formed, which have a fixed stoichiometry.<sup>20</sup> In many cases, more than one IMC structure is possible, depending on the ratio of elements. At low metal loadings, IMCs often form a thin surface alloy even in the presence of excess oxide promoter. As the amount of promoter oxide near the metallic NP increases, a full alloy NP is formed. With increasing amounts of promoter, the initial IMC may transform into promoter-rich IMC structures. 20,21 Although many bimetallic compositions have more than one possible IMC structure, often some of these are not formed under conditions typical of catalyst synthesis. The properties of promoters, for example, loading, reducibility, mobility, and so forth, of the oxide precursor are directly related to the final IMC structure and, more importantly, the surface composition. The latter, which determines the catalytic performance, may have a different structure from the average NP structure. However, precise structural determination of the catalytic surface remains a challenge due to the limitation of the traditional characterization methods. 1,27 Encouragingly, the advancements of the in situ structural characterization create new opportunities to understand these nanostructural differences and how they affect the catalytic properties.

In this study, we selected Pd-Bi bimetallic alloy NPs since these have been reported to display high acetylene hydrogenation selectivity. These catalysts are most selective at high Bi loadings and retain high selectivity at temperatures significantly higher than other catalyst compositions. The structure of the IMC and the reason for the high temperature performance, however, are not known. Herein, a series of Pd-Bi NPs supported on silica with Bi/Pd molar ratios of 0, 0.12, 0.25, 0.50, and 1.0 were prepared and characterized. Which Pd-Bi structures are formed and how these structure differences affect the catalytic performance for PDH and acetylene semihydrogenation model reactions were also determined. X-ray absorption spectroscopy (XAS), high-angle annular dark-field scanning transmission electron microscopy (HAADF-STEM), energy-dispersive X-ray analysis (EDS), absorption spectroscopy of adsorbed CO, in situ diffuse reflectance infrared Fourier transform (DRIFTS), and X-ray photoelectron spectroscopy (XPS) were employed to identify the surface structure and NP composition of the Pd-Bi catalysts. As the Bi loading increased, there was an evolution on the surface and bulk NP structures, which led to changes in the catalytic performances, for example, selectivity, rate, and deactivation. The adjacent Pd atoms in the Pd-Bi alloy are spatially isolated, which suppress the hydrogenolysis rate, leading to the significantly improved selectivity for PDH and acetylene semihydrogenation reactions. Importantly, as demonstrated in this study, the catalyst performance is not only determined by the alloy structure but can also be significantly affected by the amount of noncatalytic oxide promoter which can cover the active sites, leading to low rates.

#### 2. EXPERIMENTAL SECTION

**2.1. Catalyst Synthesis.** A monometallic 2 wt % Pd catalyst (supported on Davisil Grade 646 silica gel, Sigma-Aldrich, 35-60 mesh, pore volume 1.15 cm³/g) was synthesized using the incipient wetness impregnation (IWI) method. Pd(NH<sub>3</sub>)<sub>4</sub>(NO<sub>3</sub>)<sub>2</sub> solution (Sigma-Aldrich, 1.126 g, 10%) was diluted with 0.8 mL of H<sub>2</sub>O. Ammonium hydroxide solution (Sigma-Aldrich, 0.2 mL, 30%) was then added to the solution until the pH reached 11. The obtained Pd precursor was added dropwise to 2 g of silica with continuous stirring. After drying overnight at 125 °C, the sample was calcined at 400 °C for 3 h and reduced at 200 °C in 5% H<sub>2</sub>/N<sub>2</sub> at 100 cm³ min<sup>-1</sup> for 30 min.

A series of SiO<sub>2</sub>-supported Pd-Bi bimetallic catalysts containing 2 wt % Pd with Bi/Pd molar ratios of 0.12:1, 0.25:1, 0.50:1, and 1:1 were synthesized by a sequential IWI (s-IWI). The Pd-Bi/SiO<sub>2</sub> samples were denoted based on their target Bi/Pd molar ratios. A similar synthesis procedure was applied to all the catalysts. For example, Pd-Bi/SiO<sub>2</sub>-0.25 was prepared by dissolving 1.126 g of  $Pd(NH_3)_4(NO_3)_2$  (10 wt %) in 0.7 mL of deionized water. Ammonium hydroxide solution (Sigma-Aldrich, 0.2 mL, 30%) was then added to the solution until the pH reached 11, which was then added to 2 g of SiO<sub>2</sub>, dried at 125 °C, and calcined at 400 °C for 4 h to give Pd/SiO<sub>2</sub> NPs. Bi(NO<sub>3</sub>)<sub>3</sub>·5H<sub>2</sub>O (0.0464 g) (Alfa Aesar) was dissolved in 2 mL of 2 mol/L nitric acid and was added dropwise to the abovementioned Pd/SiO<sub>2</sub>. Next, the catalyst was dried overnight at 125 °C, calcined for 4 h at 400 °C, reduced at 200 °C in 5%  $H_2/N_2$  at 100 cm<sup>3</sup> min<sup>-1</sup> for 30 min, and then reduced at 550 °C in 5% H<sub>2</sub>/N<sub>2</sub> at 100 cm<sup>3</sup> min<sup>-1</sup> for 30 min. The Pd $-Bi/SiO_2$ -0.12, Pd $-Bi/SiO_2$ -0.50, and Pd $-Bi/SiO_2$ -0.50 SiO<sub>2</sub>-1.0 samples were prepared by the same method by adding 0.0232, 0.0928, and 0.1856 g of the  $Bi(NO_3)_3 \cdot 5H_2O_7$ respectively.

**2.2.** Characterization. 2.2.1. DRIFTS of CO Chemisorption. In situ DRIFT spectra were collected on a Nicolet iS50 spectrometer with a mercury cadmium telluride (MCT) detector cooled by liquid nitrogen. Prior to the test,  $\sim$ 20 mg of the sample was reduced at 550 °C under 10 vol % H<sub>2</sub> for 30 min, and the background spectrum was collected after purging with N<sub>2</sub> at room temperature for 40 min. Then the prereduced samples were exposed to 10 vol % CO in N<sub>2</sub> at 25 °C for 20 min, and the sample IR spectra were collected after purging with N<sub>2</sub> for 40 min.

2.2.2. Aberration-Corrected Scanning Transmission Electron Microscopy (AC-STEM). Atomic resolution microscopy analysis, as well as elemental mapping, was performed on the JEM ARM200F microscope working at 200 kV with a probe Cs-corrector at Dalian Institute of Chemical Physics, Chinese Academy of Sciences (DICP, CAS). For HAADF imaging, a convergence angle of ~23 mrad and a collection angle range of 68-174 mrad were adapted for incoherent imaging, providing characteristic high contrast between Pd- and Bi-rich atomic columns. The PdBi sample composition, as well as element spatial distribution, was studied using an energy-dispersive Xray analyzer (EX-230 100 mm<sup>2</sup> detector) equipped on ARM200F. For the microscopy sample preparation, the four  $Pd-Bi/SiO_2-n$  (n = 0.12, 0.25, 0.50, and 1.0) catalysts were dispersed in ethanol and dropped onto the copper grids and dried on a hot plate for 5 min (150 °C). Particle size

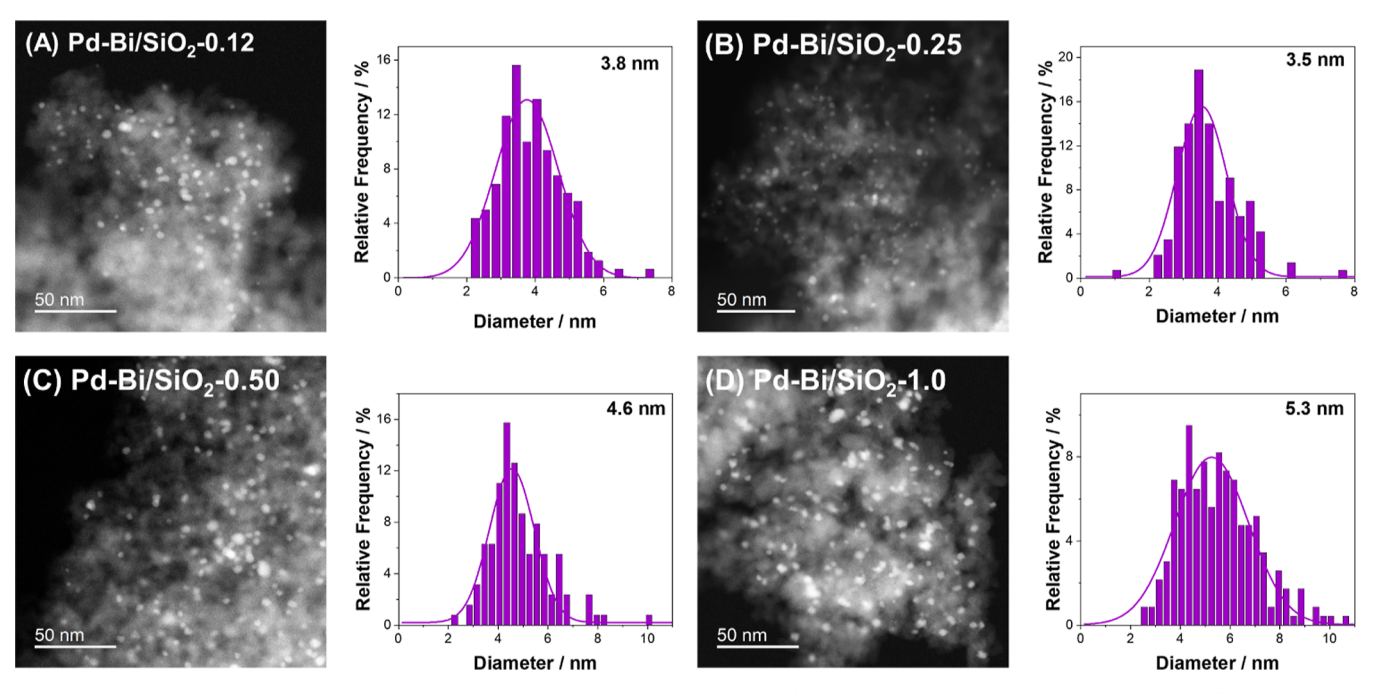


Figure 1. TEM micrographs and histograms of metal particle size distribution for (A) Pd-Bi/SiO<sub>2</sub>-0.12, (B) Pd-Bi/SiO<sub>2</sub>-0.25, (C) Pd-Bi/SiO<sub>2</sub>-0.50, and (D) Pd-Bi/SiO<sub>2</sub>-1.0 samples.

distribution was determined by counting more than 100 particles per sample using Nano Measurer 1.2.

2.2.3. In Situ XAS. XAS measurements at the Pd K-edge (24350 eV) were performed on the 10-BM bending magnet beamline of the Materials Research Collaborative Access Team (MRCAT) at the Advanced Photon Source (APS), Argonne National Laboratory. Measurements were taken in the transmission mode using three ion chambers which allowed for simultaneous measurement of a Pd foil for energy calibration. Samples were ground into fine powders and pressed inside of a cylindrical sample holder and sealed in a sample cell allowing for gas flow. Before the XAS spectra were obtained, the catalysts were reduced at 550 °C in a 5% H<sub>2</sub>/He mixture for 30 min. After reduction, the samples were purged with He at 100 cm<sup>3</sup> min<sup>-1</sup> and cooled to room temperature. Trace oxidants in He were removed by passing through a Matheson PUR-Gas Triple Purifier Cartridge containing a Cu trap. All spectra were obtained at room temperature in He.

WinXAS 3.1 software was used to analyze the XAS spectra. The edge energy was determined using the maximum of the first peak in the first derivative of the X-ray absorption nearedge structure (XANES) spectra. Least-squares fitting was performed in the R space of the  $k^2$ -weighted Fourier transform (FT) data on isolated first shell scattering for each sample. Each sample was fit using two scattering paths (Pd–Pd and Pd–Bi). Feff6 calculations were used to fit Pd–Pd and Pd–Bi scattering pairs. <sup>28,29</sup> The  $S_0^2$  was fixed at 0.836 in the standard fitting procedures to find the coordination number (CN) and bond distances between Pd and its neighbors. The  $\Delta\sigma^2$  value was held constant for all samples, while the CN, bond distance, and  $E_0$  correction were varied to determine the best fit.

2.2.4. In Situ XPS. For quasi in situ XPS experiments, the samples were first compacted into a wafer with a diameter of 5 mm, and then, the wafer was reduced in a in situ reactor cell equipped in XPS (Thermo Fisher ESCALAB Xi+ XPS, monochromatic Al source) under 10%  $\rm H_2/He$  at 550 °C for 0.5 h. The reduced samples were transferred into the analysis

chamber, and the data were recorded under ultrahigh vacuum (5  $\times$  10<sup>-7</sup> Pa). All spectra were calibrated to the graphitic carbon peak of C 1s at 284.8 eV and further analyzed using the software package of CasaXPS (version 2.3.19).

2.3. Catalyst Evaluation. Catalysts were tested on two model reactions, PDH and acetylene semihydrogenation. The catalytic performance was indicative of changes on the catalytic surface with changing composition. PDH was conducted in a fixed-bed quartz tube (3/8 in. OD) microreactor. The loaded catalysts were varied from 30 to 1000 mg to vary the initial propane conversion, and the total mass was diluted with SiO<sub>2</sub> to 1.0 g, which is around 5 cm in the height of the catalyst bed. A thermocouple (O.D. = 3.2 mm) was placed at the center of the catalyst bed to measure the reaction temperature. Within 5 °C temperature variation was observed along the catalyst bed. Before the reaction, the catalysts were reduced at 550 °C with 5% H<sub>2</sub> (100 mL/min) for 30 min. Before starting the flow of reactant gasses, hydrogen was purged from the bed by flowing 100 mL/min nitrogen for 5 min. PDH reactions were carried out at 550 °C with 2.5% propane and 2.5% hydrogen. A broad range of conversion was obtained by changing the total flow rate and mass of the catalyst. Each conversion/selectivity data point was collected on a fresh sample. Gas chromatograph (Agilent 6890) with an FID detector and a Restek Alumina BOND/Na2SO4 GC column was used to determine the amount of propane, propylene, methane, ethane, and ethylene. The propane conversion and propylene selectivity were calculated using the equations below.

Conv (%) =

moles of propane in inlet — moles of propane in outlet

moles of propane in inlet

× 100%

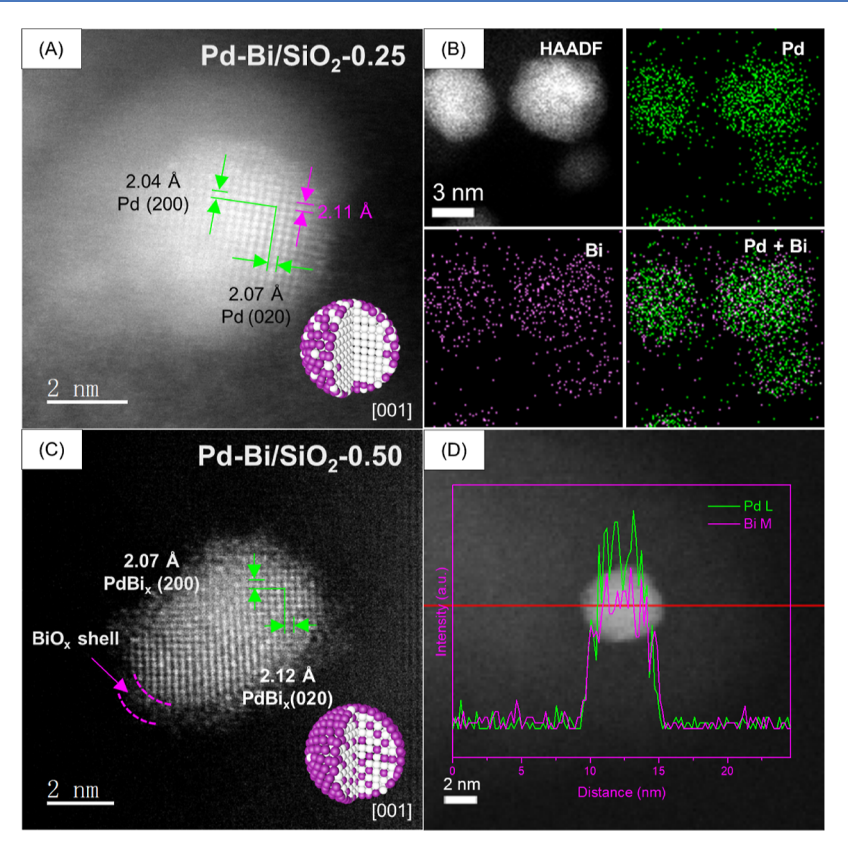


Figure 2. High-resolution HAADF imaging and elemental composition analysis of Pd-Bi/SiO<sub>2</sub>-0.25 (A,B) and Pd-Bi/SiO<sub>2</sub>-0.50 (C,D), respectively.

Sel (%)
$$= \frac{\text{moles of propylene}}{\text{moles of propylene} + \frac{2 \times \text{moles of C2}}{3} + \frac{\text{moles of CH}_{4}}{3}}$$

The apparent activation energy  $(E_{\rm a})$  was determined by Arrhenius plots below 10% propane conversion under each reaction temperature.

The deactivation rate constant  $(k_d)$ , as the equation shown below, was determined using the first-order model.

$$k_{\rm d} = \frac{\ln\left(\frac{100 - \text{Conv}_{\rm I}}{\text{Conv}_{\rm I}}\right) - \ln\left(\frac{100 - \text{Conv}_{\rm 0}}{\text{Conv}_{\rm 0}}\right)}{t}$$

where  $Conv_1$  and  $Conv_0$  are the final and initial propane conversions, respectively. t is the duration of reaction (40 h), and  $k_d$  is the deactivation constant ( $h^{-1}$ ).

Acetylene semihydrogenation was carried out in a quartz tube (6 mm OD and 4.35 mm ID) with glass wool plugs on each side to retain the catalyst. A 1 wt %  $Pd/Al_2O_3$  catalyst was used as a reference to contrast the performance of the  $Pd-Bi/SiO_2$ . A thermocouple was placed in the catalyst bed to measure the reaction temperature. The catalysts were reduced for 60 min at 350 °C with 13 mL/min  $H_2$ . The reactant gas was composed of 1%  $C_2H_2$ , 4%  $H_2$ , and the rest balanced with  $N_2$  at a total flow rate of 50 mL/min. Acetylene conversion and ethylene selectivity were calculated as shown below

acetylene conversion (%)  $= \frac{\text{moles of C}_2H_4 \text{ in outlet } + \text{moles of C}_2H_6 \text{ in outlet}}{\text{moles of C}_2H_2 \text{ in inlet}} \times 100\%$  ethylene selectivity (%)  $= \frac{\text{moles of C}_2H_4 \text{ in outlet}}{\text{moles of C}_2H_4 \text{ in outlet}} \times 100\%$ 

## 3. RESULTS

× 100%

**3.1. TEM.** The morphology and size distribution of the reduced Pd-Bi bimetallic catalysts were characterized by TEM. Figure 1A-D shows the typical TEM images and corresponding size distribution. The particle size distributions were obtained by randomly selecting 100-200 NPs for each catalyst. All the sizes of NPs are in the range of 3-5 nm. The similar particle sizes of these catalysts enable comparison between their catalytic performance and surface structure without having to account for the changes in particle size. For comparison, the monometallic Pd/SiO<sub>2</sub> NPs have a slightly smaller average particle size ( $\sim 1.7$  nm), as shown in Figure S1.

**3.2. HAADF–STEM.** High-resolution HAADF–STEM imaging (Figure 2) provides structural details of Pd–Bi catalysts in localized real space. Figure 2A,C show the atomic structure oriented along the [001] zone axis of Pd–Bi/SiO<sub>2</sub>-0.25 and Pd–Bi/SiO<sub>2</sub>-0.50 in typically ~4 nm NPs, respectively. In Pd–Bi/SiO<sub>2</sub>-0.25, the lattice spacing at the NP exterior, 2.11 Å, and interior, 2.04 Å, indicate a two-phase

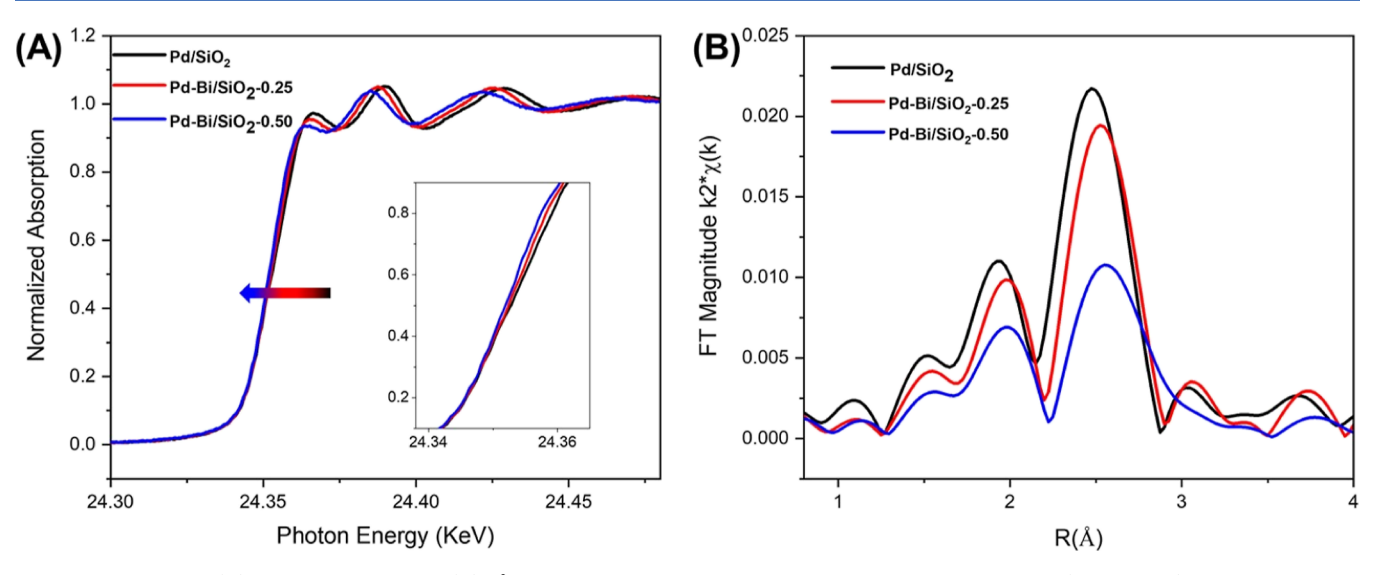


Figure 3. Pd K-edge (A) XANES spectra and (B)  $k^2$ -weighted magnitude of the FT of the EXAFS for Pd/SiO<sub>2</sub> (black curve), Pd-Bi/SiO<sub>2</sub>-0.25 (red curve), and Pd-Bi/SiO<sub>2</sub>-0.50 (blue curve) samples.

Table 1. XAS Pd K-Edge Fits of the Reduced Pd and Pd-Bi Catalysts

catalyst	scattering pairs	XANES energy (keV)	CN	R (Å)	$\Delta\sigma^2$	$E_0$ (eV)
Pd/SiO <sub>2</sub>	Pd-Pd	24.3500	8.3	2.73	0.007	-1.0
$Pd-Bi/SiO_2-0.25$	Pd-Pd	24.3494	8.3	2.77	0.007	-1.2
	Pd-Bi		2.4	2.83	0.007	2.1
Pd-Bi/SiO <sub>2</sub> -0.25 (three-shell fit)	Pd-Pd	24.3494	3.6	2.73	0.007	-1.0
	Pd-Pd		4.7	2.80	0.007	-1.3
	Pd-Bi		2.3	2.83	0.007	2.1
$Pd-Bi/SiO_2-0.50$	Pd-Pd	24.3489	5.8	2.80	0.007	-1.6
	Pd-Bi		3.3	2.83	0.007	-0.4

morphology with a Pd core and Pd–Bi IMC shell. The Pd EDS signal displays a thickness-dependent distribution over the Pd–Bi/SiO<sub>2</sub>-0.25 catalyst (Figure 2B), whereas the EDS signal of bismuth has uniform intensity to the projected thickness. Such EDS results, as well as the lattice spacing expansion (from 2.04 to 2.11 Å) on the particle surface, are consistent with a metallic Pd core covered by a Pd–Bi alloy shell (Figure 2A,B).

For the Pd–Bi/SiO<sub>2</sub>-0.50 catalyst (Figure 2C), the crystal lattice is similar to the surface phase in Pd–Bi/SiO<sub>2</sub>-0.25, that is, 2.12 Å. In this sample, the lattice expansion was found throughout the particle, suggesting that a full alloy is formed, that is, no Pd core. An EDS line-distribution of Pd and Bi across the NP further supports the formation of a Pd–Bi alloy phase (Figure 2D). In Figure 2C, there is also evidence of an amorphous BiO<sub>x</sub> shell on the NP surface with a thickness of about 0.5 nm, which appears to cover the NP's surface.

**3.3. XAS.** To further verify the structural differences with increasing Bi-level, XAS was carried out to evaluate the local coordination environment. XANES spectra were obtained at Pd K-edge (24350 eV) for Pd-Bi and Pd NP catalysts. The XANES spectra are shown in Figure 3A, and the edge energies are listed in Table 1. All measurements were taken at room temperature under He atmosphere after reduction at 550 °C. The monometallic Pd NPs have a spectral shape, white line intensity, and edge energy (24,350.0 eV) similar to that of the Pd foil, suggesting that the Pd atoms are fully reduced. For the Pd-Bi/SiO<sub>2</sub>-0.25 catalyst, there is a slight decrease in the white line and a small shift to lower edge energy (24,349.4 eV, Table 1), which suggests the presence of other metallic atoms

in the Pd–Bi NPs.  $^{30}$  As the Bi loading increases, for example, in Pd–Bi/SiO<sub>2</sub>-0.50, there is a further decrease in white line intensity and a shift to lower edge energy (24,348.9 eV), indicating a higher level of Bi within the Pd bonding distance.  $^{31}$ 

The Pd K-edge extended X-ray absorption fine structure (EXAFS) spectra show the same trend observed with the XANES spectra, that is, with increasing Bi loading in the catalysts, there is increasing amounts of Bi in the alloy NPs. Since EXAFS spectroscopy measures all the surface and interior atoms in the sample, it is difficult to identify the surface structure, especially when multiple phases may be formed, for example, core—shell, IMC, or solid solution. Therefore, it is also necessary to determine the surface composition and structure, which are responsible for the catalytic performance.

Figure 3B shows the  $k^2$ -weighted magnitudes of the FT of the EXAFS spectra. The fitting results are summarized in Table 1. The first shell magnitude of the FT of Pd/SiO $_2$  shows two prominent peaks with one large peak at  $\sim$ 2.4 Å and a smaller peak at  $\sim$ 1.9 Å (phase-uncorrected distances), which is typical of metallic Pd NPs. The Pd-Pd CN in Pd/SiO $_2$  was fitted to be 8.3 at 2.73 Å, while Pd-Pd CN is 12 at 2.75 Å in the Pd foil. The smaller Pd-Pd CN and the shorter Pd-Pd bond distance of Pd NPs are consistent with 3.2 nm Pd NPs, 33 which agrees with the averaged size from STEM analysis.

Although the STEM size of Pd-Bi NPs is larger than that of Pd NPs, the magnitude of the FT is smaller and is shifted to a slightly longer distance, which suggests an additional Pd-Bi scattering path and the formation of Pd-Bi IMCs. The

scattering from the heavier atom, that is, Bi (and at a longer distance, see fittings in Table 1), leads to destructive interference and reduction of the EXAFS magnitude. The Pd K-edge EXAFS spectra were fit to determine the average coordination of Pd neighbors, and the results are shown in Table 1. For Pd-Bi/SiO<sub>2</sub>-0.25, the Pd-Pd CN is 8.3 at a bond distance of 2.77 Å and the Pd-Bi CN is 2.4 at 2.83 Å. The Pd-Pd bond distance is longer than that in Pd NPs (2.73 Å) and Pd foil (2.75 Å).

As the Bi loading in the catalyst increases, the shape in the magnitude of the FT of the EXAFS spectrum of Pd-Bi/SiO<sub>2</sub>-0.50 changes and shifts to a slightly longer distance consistent with more Bi in the alloyed NP. The Pd-Pd CN decreases to 5.8 at a bond distance of 2.80 Å, and the Pd-Bi CN increases to 3.3 at 2.83 Å, which is similar to the Pd-Bi bond distance in Pd-Bi/SiO<sub>2</sub>-0.25. The Pd-Pd bond distance (2.80 Å) in the Pd-Bi/SiO<sub>2</sub>-0.50 is significantly longer than that in Pd NPs (2.73 Å). The CN ratios (Pd-Pd/Pd-Bi coordination ratio = 1.8) of this catalyst are very similar to that of the Pd<sub>3</sub>Bi IMC (Pd-Pd/Pd-Bi coordination ratio = 2.0). In a bulk alloy, the Pd-Pd and Pd-Bi bond distances are 2.87 and 2.86 Å, respectively, and the Pd-Pd/Pd-Bi coordination ratio is 8/4. In NPs, the bond distances are slightly smaller than those in bulk alloys and the CN ratio is the same as bulk but with lower values

Since the Pd–Pd/Pd–Bi coordination ratio of the Pd–Bi/SiO<sub>2</sub>-0.25 was about 3.5, that is, greater than 2, and the STEM results showed a Pd core-Pd-Bi IMC surface, the Pd–Pd scattering path was likely from two phases with different Pd–Pd bond distances. Thus a three-shell fit of this catalyst was obtained. The Pd–Pd bond distance of the core was fixed at the same bond distance of the Pd NP, that is, 2.73 Å, while the Pd–Pd bond distance in the surface Pd–Bi IMC was fixed at 2.80 Å, the same as that in the Pd<sub>3</sub>Bi IMC in Pd–Bi/SiO<sub>2</sub>-0.50. The three-shell fit gave a Pd–Pd CN of 3.6 at 2.73 Å for the metallic Pd core, with a Pd–Pd CN of 4.7 at 2.80 Å and Pd–Bi at 2.83 Å. Within the errors of the EXAFS fits, Pd–Pd/Pd–Bi coordination ratio of the surface alloy was close to 2, consistent with that in the Pd<sub>3</sub>Bi IMC.

**3.4. DRIFTS of CO Chemisorption.** Figure 4 shows the IR spectra of adsorbed CO at saturation coverage for all four Pd—Bi catalysts and the monometallic Pd NPs. The 2 wt % Pd/  $SiO_2$  catalyst shows a typical spectrum for small, monometallic

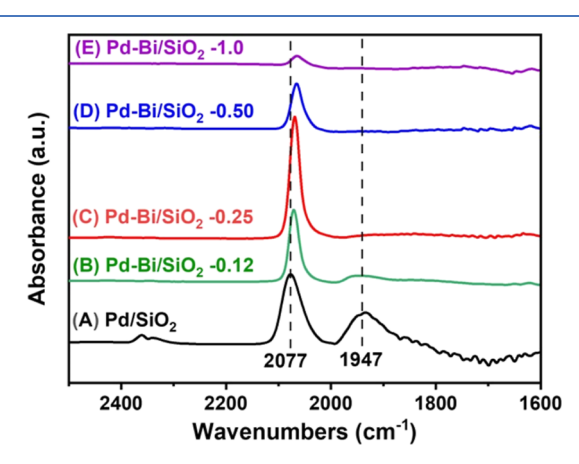


**Figure 4.** FT CO-IR spectra of reduced (A) Pd/SiO<sub>2</sub>, (B) Pd-Bi/SiO<sub>2</sub>-0.12, (C) Pd-Bi/SiO<sub>2</sub>-0.25, (D) Pd-Bi/SiO<sub>2</sub>-0.50, and (E) Pd-Bi/SiO<sub>2</sub>-1.0.

Pd NPs, where CO binds in both linear (2077 cm<sup>-1</sup>) and bridge (1947 cm<sup>-1</sup>) fashion.<sup>34,35</sup> The bridge-to-linear ratio for the catalysts was determined by dividing the total peak area between 1800 and 2000 cm<sup>-1</sup> by the peak area between 2000 and 2100 cm<sup>-1</sup>, as shown in Table 2. Although this ratio does not take into consideration the extinction coefficients of the different CO adsorption bands and is not, therefore, quantitatively related to the CO coverages of the various Pd sites, the ratio does reflect qualitative changes in the surface of the catalyst.<sup>31</sup> The monometallic Pd catalyst has a bridge-to-linear ratio of 0.73 (Table 2), which is consistent with previous studies of small Pd NPs (~2 nm).<sup>21,31</sup>

The Pd-Bi alloy NPs are slightly larger than those of monometallic Pd; however, Pd NPs (4-5 nm) have increased the bridge-to-linear-bonded CO peak ratio, for example, smaller linear- and much larger bridge-bonded, than that of 2 nm size particles. The addition of Bi and formation of Pd-Bi IMCs decrease the bridge-to-linear ratio to 0.28 for the Pd-Bi/SiO<sub>2</sub>-0.12 and further to 0.14 for Pd-Bi/SiO<sub>2</sub>-0.25 (Table 2), suggesting a decrease in the surface Pd ensemble size. In Figure 4, at the lowest Bi loading in Pd-Bi/SiO<sub>2</sub>-0.12, there are few sites which can bridge-bound CO, while in Pd-Bi/ SiO<sub>2</sub>-0.25, the bridge-bound CO peak is nearly absent. This likely results from the elongated Pd-Pd distance in Pd-Bi IMCs, as evidenced in the XAS fitting (2.80 Å vs 2.73 Å in monometallic Pd NPs), and provides further evidence for the formation of Pd-Bi IMCs on the surface of Pd-Bi catalysts, leading to the spatially isolated Pd sites. A similar loss of the bridge-bound CO peak has been observed in Ni<sub>3</sub>Sn/SiO<sub>2</sub>, <sup>30</sup> Ni<sub>3</sub>Ge/SiO<sub>2</sub>,<sup>37</sup> and Pt<sub>3</sub>Sn/H-SAPO-11<sup>38</sup> due to the greater atomic distance between Ni or Pt atoms in these IMCs.

At high Bi loadings, only linearly adsorbed CO is observed; however, its intensity decreases with increasing Bi loading in Pd-Bi/SiO<sub>2</sub>-0.50 and Pd-Bi/SiO<sub>2</sub>-1.0. For the latter, little CO is adsorbed, suggesting a high coverage of the Pd-Bi alloy surface, likely by excess Bi species observed by STEM.

In addition to the loss of bridge-bonded CO in the IR spectra of Pd-Bi catalysts, there is a shift to lower frequency of the linear-bound CO peak with increasing Bi loading. For example, the linear-bonded CO shifts from 2077 cm<sup>-1</sup> in monometallic Pd NPs to 2065 cm<sup>-1</sup> for Pd-Bi/SiO<sub>2</sub>-0.50. The frequency of the linear-bonded CO for all catalysts is given in Table 2. This shift to lower frequency could be attributed to the coverage-induced frequency shift. Specifically, the frequency of adsorbed CO increases with increasing surface coverage due to the dipole-dipole coupling. At high CO coverage on monometallic Pd NPs, the linear CO frequency is 2077 cm<sup>-1</sup>. For the Pd<sub>3</sub>Bi, the Pd–Pd distance is much longer than that in Pd NPs, for example, 2.80 verses 2.73 Å in Pd NPs. The longer Pd-Pd nonbonding distance and geometrical isolation of Pd by Bi in the Pd-Bi IMCs would be expected to reduce the CO dipole interactions, leading to the red shift in IR spectra. This shift to lower frequency in the linear adsorbed CO is consistent with previous IR studies. 39-44 Finally, while there was a small bridge-bonded CO peak in Pd-Bi/SiO<sub>2</sub>-0.12, there was also a shift in the frequency of the linear peak, suggesting that the surface has regions of both monometallic Pd and partial coverage by the Pd<sub>3</sub>Bi IMC.

**3.5. XPS.** The *in situ* Pd XPS spectra for Pd/SiO<sub>2</sub>, Pd-Bi/SiO<sub>2</sub>-0.25, and Pd-Bi/SiO<sub>2</sub>-0.50 NPs are shown in Figure S2. Two distinct peaks at around 335.8 and 341.1 eV are in accordance with the reported literature values for Pd  $3d_{5/2}$  and Pd  $3d_{3/2}$  of Pd(0) NPs, respectively.<sup>45–47</sup> For all catalysts, the

Table 2. Catalytic Performance and Kinetics Parameters of PDH (2.5% C<sub>3</sub>H<sub>8</sub> and 2.5% H<sub>2</sub> Balanced in N<sub>2</sub> at 1 atm and 550 °C)

catalyst	liner peak position $(cm^{-1})$	bridge/linear ratio (IR)	STEM size (nm)	fraction of surface Pd <sup>a</sup> (%)	propylene selectivity (%)	PDH rate per surface $Pd^{c}(10^{-3})$	$(h^{-1})$	$E_{\rm a}$ (kJ/mol)
Pd/SiO <sub>2</sub>	2077	0.73	1.7	59	44	8.2	0.14	93
$Pd-Bi/SiO_2-0.12$	2071	0.28	3.8	26	71	13.3	0.08	
$Pd-Bi/SiO_2-0.25$	2069	0.14	3.5	29	95	14.3	0.04	129
$Pd-Bi/SiO_2-0.50$	2065	0	4.6	22	95	1.1		139
Pd-Bi/SiO <sub>2</sub> -1.0	2064	0	5.3	19	95	0.4		

<sup>&</sup>quot;All catalysts contain 2 wt % Pd. The fraction of surface Pd was calculated from NP size, 1/diameter (nm). The selectivity was measured at 25% propane conversion from the initial t = 0 value. The PDH rate/moles of surface Pd (moles  $C_3H_6/\text{mole}$  surface Pd/s) was determined at 10%  $C_3H_8$  conversion.

 $3d_{5/2}$  and  $3d_{3/2}$  B.E.s are the same within error. Additionally, Pd  $4f_{5/2}$  B.E. of Pd and Pd-Bi catalysts was also the same at  $162.4 \pm 0.1$  eV. The Pd  $3d_{5/2}$  and Pd  $3d_{3/2}$  B.E. are slightly higher than those of Pd bulk metal (335.1 eV), due to the decreased extra-atomic relaxation of small metal particles. Although the reduced catalysts were evacuated at 400 °C, in the *in situ* Pd XPS spectra for Pd/SiO<sub>2</sub>, there is, perhaps, a small, higher energy shoulder of the Pd  $3d_{5/2}$  and Pd  $3d_{3/2}$  peaks, for example, 336.8 and 342.6 eV  $\pm$  0.1 eV, respectively. These higher B.E. peaks have been associated with PdH<sub>x</sub>. <sup>49</sup> For Pd-Bi/SiO<sub>2</sub>-0.25, there is a smaller 335.8  $\pm$  0.1 eV peak, suggesting less PdH<sub>x</sub>, while for Pd-Bi/SiO<sub>2</sub>-0.50, this peak is absent. The fractional composition of each species is given in Table S1. The results suggest that the formation of Pd<sub>3</sub>Bi does not form PdH<sub>x</sub>.

**3.6.** Catalytic Performance for PDH. Pd—Bi catalysts were evaluated together with the monometallic Pd catalyst for PDH in a mixture of 2.5% C<sub>3</sub>H<sub>8</sub> and 2.5% H<sub>2</sub> with balanced N<sub>2</sub> at 550 °C after pre-reduction at 550 °C. The PDH evaluation was carried out in the presence of H<sub>2</sub> since an increase in the hydrogen-to-hydrocarbon ratio accelerates hydrogenolysis and is, therefore, a more rigorous test of propylene selectivity. The PDH products were mainly propylene with small amounts of methane, ethane, and ethylene. The latter three result from hydrogenolysis.

The experimental results are shown in Figure 5. Each data point corresponds to the conversion and selectivity from a separate catalyst test. For each test, the conversion versus selectivity was determined at short time on stream, ca. 1 min after steady-state start of run, that is, low coke selectivity. The mass of the catalyst and flow rates were varied to achieve a range of conversions up to about 30%. For Pd/SiO<sub>2</sub>, the propylene selectivity is around 62% at about 7% propane conversion, which decreases rapidly to about 41% at 32% propane conversion. The propylene selectivity declines rapidly as a function of increasing conversion, which is consistent with literature reports of monometallic Pd catalysts. <sup>9,20,21,31</sup>

The Pd–Bi catalysts showed a different trend in propylene selectivity compared to that of monometallic Pd (Table 2). Because chemical reactions occur on the catalyst surface, the subtle differences in propylene selectivity suggest the surface composition changes with increasing Bi-level. On adding a small amount of Bi, for example, Pd–Bi/SiO<sub>2</sub>-0.12, the propylene selectivity at any conversion is improved compared with that of monometallic Pd NPs but decreases rapidly with increasing conversion similar to that of Pd NPs (Figure 5), suggesting that the surface has both Pd and Pd<sub>3</sub>Bi IMC regions. This is consistent with the DRIFTS spectrum, where small bridge-bonded CO peak as well as a shift in the

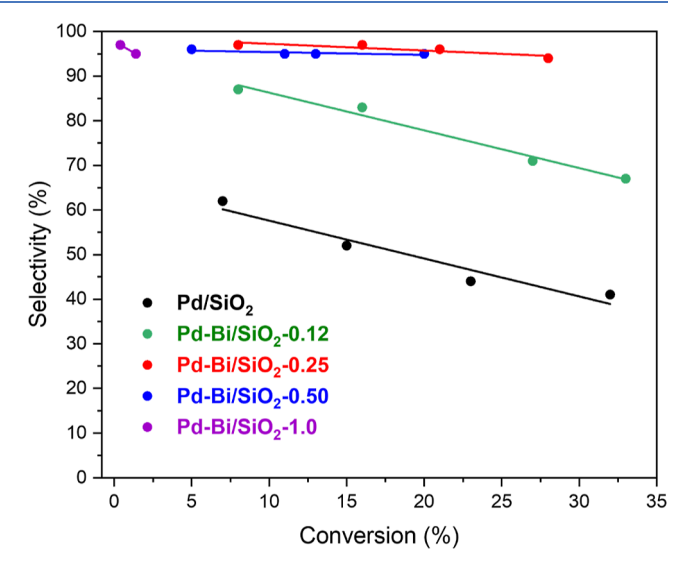


**Figure 5.** Initial propylene selectivity versus propane conversion for Pd—Bi catalysts in PDH reaction at 550  $^{\circ}$ C compared with that of the monometallic Pd catalyst in 2.5%  $C_3H_8$  and 2.5%  $H_2$  with balanced N.

frequency of the linear peak were observed. At 35% propane conversion, the propylene selectivity increases to 66%, about 25% higher than that of Pd NPs (41%).

With slightly higher Bi content, Pd-Bi/SiO<sub>2</sub>-0.25, the propylene selectivity increases to about 95% (Figure 5) and remains nearly constant from 8% to 28% propane conversion. Pd-Bi/SiO<sub>2</sub>-0.50 exhibits similar propylene selectivity at ~95% at all propane conversions, suggesting a similar surface structure. At even higher Bi loadings, Pd-Bi/SiO<sub>2</sub>-1.0, the selectivity is high; however, there is very little activity. Since the NPs are small, this suggests that there are few surface Pd sites consistent with the infrared spectrum. It is likely that the excess BiOx component observed by STEM covered most catalytic sites on the particle surface.

The fraction of surface Pd atoms was determined by STEM calculated as 1/diameter of the NPs. Table 2 gives the rates/surface Pd for each catalyst. For Pd NPs, the rate is  $8.2 \times 10^{-3}$  mol of propylene/moles of surface Pd/s. The rate of Pd-Bi/SiO<sub>2</sub>-0.25 is slightly higher, ca. 1.7 times, than that of Pd NPs. While the rate of Pd-Bi/SiO<sub>2</sub>-0.25 is very similar to that of Pd NPs, the rate of Pd-Bi/SiO<sub>2</sub>-0.5 is much lower. For example, the former has a rate of  $1.1 \times 10^{-3}$  mol of propylene/moles of surface Pd/s, which is about 8% the rate of Pd-Bi/SiO<sub>2</sub>-0.25 despite the same NP surface composition (STEM in Figure 2A,C and the EXAFS analysis in Table 1). The estimation of the number of surface Pd assumes that all surface Pd atoms are

available for reaction; however, the low rate of Pd–Bi/SiO<sub>2</sub>-0.5 is consistent with more than 90% of the surface Pd sites covered by the excess Bi oxide observed by STEM. For Pd–Bi/SiO<sub>2</sub>-1.0, the rate is even lower, 0.4  $\times$  10<sup>-3</sup> mol of propylene/moles of surface Pd/s, suggesting that about 95% of the surface is covered by excess Bi oxide.

From the abovementioned PDH results,  $Pd-Bi/SiO_2$ -0.25 and  $Pd-Bi/SiO_2$ -0.50 had very similar selectivity, while the rate of the latter was much lower. To further evaluate the surface structure of these two catalysts, the apparent activation energy of these two catalysts were measured and compared with Pd NPs. The apparent activation energy ( $E_a$ ) measured at 10% propane conversion was obtained by plotting ln(rate/g surface Pd) versus 1/T (Figure 6). The  $E_a$  for Pd NPs is 93 kJ/

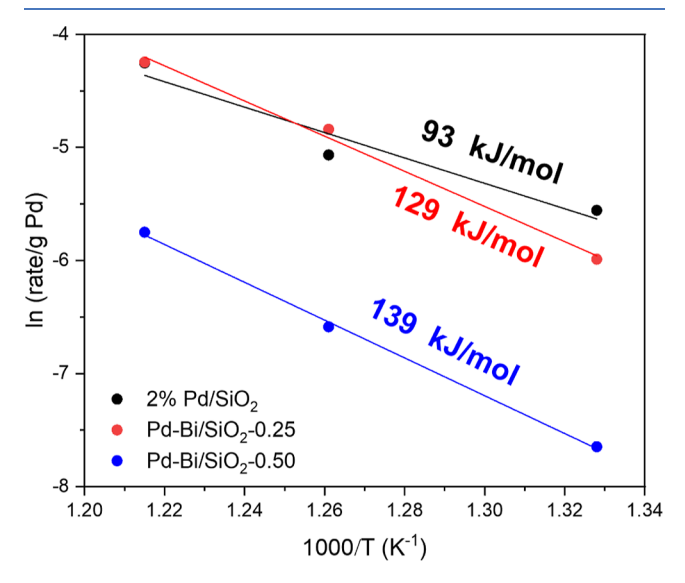


**Figure 6.** Arrhenius plots of PDH over monometallic Pd (black), Pd–Bi/SiO<sub>2</sub>-0.25 (red), and the Pd–Bi/SiO<sub>2</sub>-0.50 (blue) catalysts.

mol similar to the previously reported values for Pd NPs. The  $E_a$  values of Pd-Bi/SiO<sub>2</sub>-0.25 and Pd-Bi/SiO<sub>2</sub>-0.50 are higher with similar values at 129 kJ/mol and 139 kJ/mol, respectively. The similar  $E_a$  suggests that despite the large changes in rates, the active sites in both catalysts are similar. Thus, the similar PDH selectivity,  $E_a$ , STEM, XAS surface structure, and IR spectra are all consistent with the suggestion that these two catalysts have a similar active site structure. The

low rate of Pd-Bi/SiO<sub>2</sub>-0.50, therefore, are resulted from the loss of active sites due to the coverage by Bi oxide.

Based on the PDH results,  $Pd-Bi/SiO_2-0.25$  shows the highest selectivity and rate among the Pd-Bi catalysts. Therefore, stability is further investigated on this catalyst and compared with the more Pd-rich surface samples, for example,  $Pd-Bi/SiO_2-0.12$  and Pd NPs. The first-order deactivation rate constants ( $k_d$ ) were determined for  $Pd/SiO_2$ ,  $Pd-Bi/SiO_2-0.12$ , and  $Pd-Bi/SiO_2-0.25$  catalysts. Figure 7A shows the propane conversion versus time with an initial propane conversion of around 25%. For all catalysts, the propane conversion decreases rapidly within the first hour and reaches a steady-state conversion at longer times. The propylene selectivity of each catalyst increases for the first 100 min (Figure S3), likely because of the coking of nonselective hydrogenolysis sites, and ~95% propylene selectivity can be maintained on the  $Pd-Bi/SiO_2-0.25$  during the PDH reaction.

Pd/SiO $_2$  has the highest deactivation rate with a  $k_{\rm d}$  value of 0.14 h $^{-1}$  at 550 °C (Table 2). As shown in Figure 7B and Table 2, the deactivation constant decreases with increasing Bi loading. The  $k_{\rm d}$  value decreases from 0.08 h $^{-1}$  for Pd-Bi/SiO $_2$ -0.12 to 0.04 h $^{-1}$  for Pd-Bi/SiO $_2$ -0.25, which is approximately 28% of Pd NPs. The intermediate deactivation rate of the former likely results from the surface composition which has a partial surface coverage of both Pd and Pd $_3$ Bi IMCs and is consistent with the propylene selectivity and IR spectra. These results suggest that the Pd $_3$ Bi catalysts are more deactivation-resistant compared to monometallic Pd NPs.

**3.7. Catalytic Performance for Acetylene Semihydrogenation.** An additional model reaction of acetylene semihydrogenation was further conducted to determine the effect of NP surface composition and the role of excess Bi oxide on catalytic performance. Hydrogenation of acetylene yields ethylene, which can be further hydrogenated to ethane. A selective catalyst will be able to provide high concentrations of ethylene without forming ethane. Based on the abovementioned PDH results and characterizations, three Pd<sub>3</sub>Bi catalysts with higher Bi loading were further tested for acetylene semihydrogenation. Pd catalysts with high Bi loading have previously been shown to have high ethylene selectivity. So Although Pd—Bi IMCs were suggested, the specific structure was not given.

The acetylene conversion, ethylene, and ethane products are shown in Figure 8 for Pd NPs and Pd-Bi catalysts. In this study, 1 wt % Pd/Al<sub>2</sub>O<sub>3</sub> is used for the comparative reference

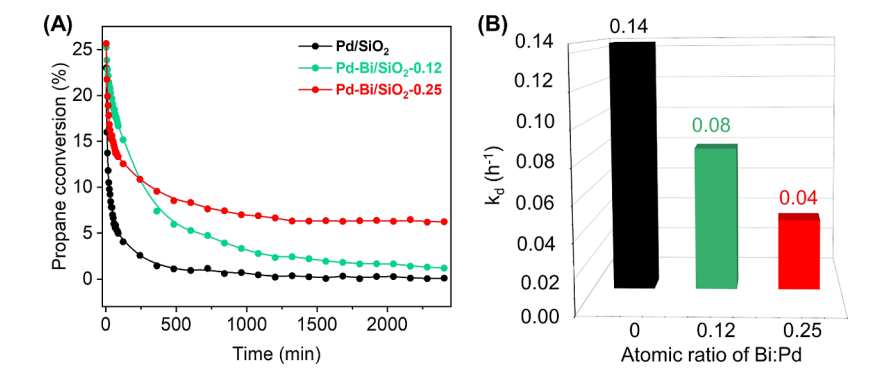


Figure 7. (A) Propane conversion during the PDH reactions and (B) corresponding deactivation constant  $k_{\rm d}$  (h<sup>-1</sup>) over Pd/SiO<sub>2</sub>, Pd-Bi/SiO<sub>2</sub>-0.12, and Pd-Bi/SiO<sub>2</sub>-0.25. [Reaction conditions: Pd/SiO<sub>2</sub> (0.027 g), Pd-Bi/SiO<sub>2</sub>-0.12 (0.36 g), and Pd-Bi/SiO<sub>2</sub>-0.25 (0.65 g); T = 550 °C; 2.5%  $C_3H_8$  and 2.5%  $H_2$  at a total flow of 200 mL/min; 1 atmospheric pressure.]

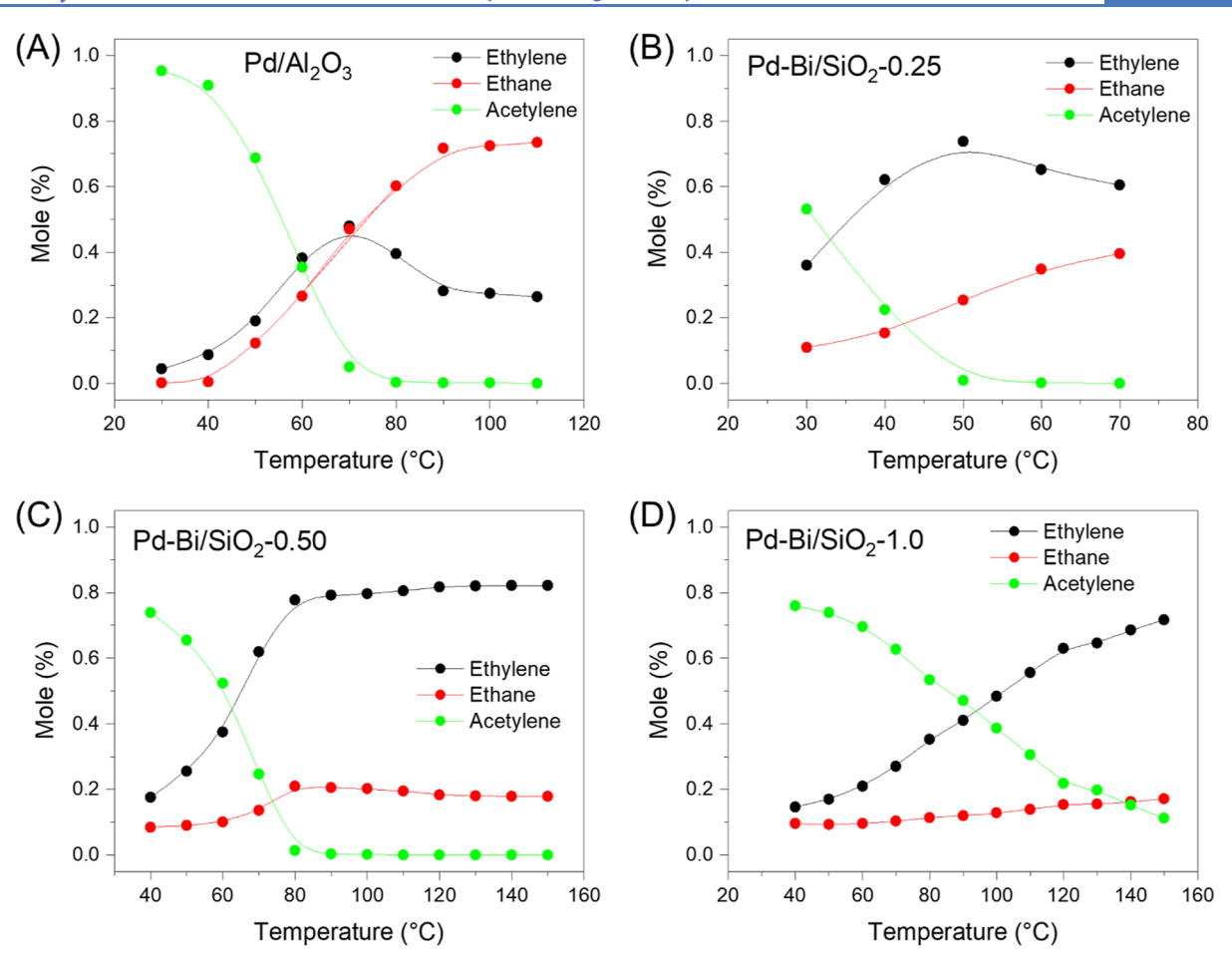


Figure 8. Concentrations of acetylene (green), ethylene (black), and ethane (red) for (A) Pd/Al<sub>2</sub>O<sub>3</sub> and (B) Pd-Bi/SiO<sub>2</sub>-0.25, (C) Pd-Bi/SiO<sub>2</sub>-0.50, and (D) Pd-Bi/SiO<sub>2</sub>-1.0 as a function of catalyst bed temperature. 20 mg of each catalyst was used for the reaction.

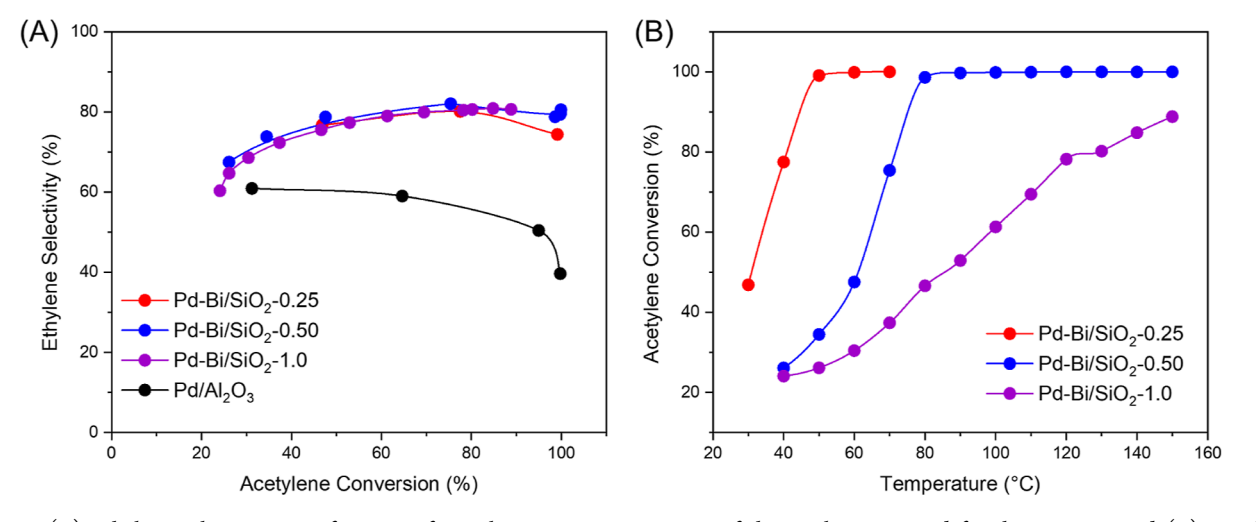


Figure 9. (A) Ethylene selectivity as a function of acetylene conversion. 20 mg of the catalyst was used for the reaction, and (B) acetylene conversion as a function of temperature.

catalyst to compare with previous literature studies. 15,50-52 However, because it has a lower Pd loading than the Bicontaining catalysts, the activity of the reference catalyst is not included in Figure 9B but is given in Figure S4. The Pd NPs form similar amounts of ethylene and ethane at low temperatures, but with increasing temperature, the amount of ethylene reaches a maximum, while ethane formation continues to increase (Figure 8A). Thus, the ethylene

selectivity falls to  $\sim 30\%$  with increasing acetylene conversion above 90% (Figure 9A). For Pd-Bi catalysts, the selectivity to ethylene exceeds that of ethane by a significant amount at all temperatures and acetylene conversions (Figure 8B-D). Therefore, by adding Bi, the ethylene selectivity increases from 30% for Pd NPs to near 80% for Pd-Bi/SiO<sub>2</sub>-0.25, Pd-Bi/SiO<sub>2</sub>-0.50, and Pd-Bi/SiO<sub>2</sub>-1.0 at near-complete acetylene conversions (Figure 9A).

The amount of Bi also affects the catalysts' activity. The conversions as a function of temperature are shown in Figure 9B and the activities are also presented as the temperature needed to achieve a 50% acetylene conversion (Table 3). The

Table 3. Catalytic Performance of Acetylene Semihydrogenation (1%  $C_2H_2$  and 4%  $H_2$  Balanced with  $N_2$  at a Total Flow Rate of 50 mL/min)

catalyst	T50 (°C) <sup>b</sup>	ethylene selectivity $(\%)^c$
Pd/Al <sub>2</sub> O <sub>3</sub> <sup>a</sup>	48	58
$Pd-Bi/SiO_2-0.25$	31	75
$Pd-Bi/SiO_2-0.50$	62	77
Pd-Bi/SiO <sub>2</sub> -1.0	83	75

 $^a$ The Pd/Al $_2$ O $_3$  had 1 wt % Pd, while the Pd—Bi catalysts have 2 wt % Pd.  $^b$ Catalyst bed temperature needed for achieving 50% acetylene conversion.  $^c$ Ethylene selectivity at 50% acetylene conversion.

temperature increases from 31  $^{\circ}$ C for the Pd–Bi/SiO<sub>2</sub>-0.25 to 62  $^{\circ}$ C for the Pd–Bi/SiO<sub>2</sub>-0.50 and 83  $^{\circ}$ C for the Pd–Bi/SiO<sub>2</sub>-1.0. These results are consistent with the changes in rate for PDH, where with increasing Bi loading, the rate/surface Pd decreases due to coverage by excess Bi content.

Figure 9 shows that catalysts with surface Pd<sub>3</sub>Bi IMC structures are more selective than Pd NP even at high acetylene conversion. As the Bi addition increases, the temperature required to obtain high conversion increases, which corresponds to the fewer number of active sites. Although high Bi loadings do allow for selectivity at higher reaction temperatures, this appears to result in the availability of fewer exposed sites.

### 4. DISCUSSION

4.1. NP and Surface Structural Evolution of Pd₃Bi. For many catalyst compositions and reactions, the formation of alloy NPs often leads to improvements in selectivity, rate, and stability compared to monometallic catalysts. As this study shows, the addition of Bi to Pd leads to improved catalytic performance for PDH and acetylene semihydrogenation. As schematically illustrated in Figure 10, the NP phase, surface composition, and accessibility to the active atoms are dependent on the amount of the promoter.

During the synthesis, both Pd and Bi oxides are dispersed on the support. Under the reducing pretreatment conditions, Pd is first reduced to Pd NPs at about 200 °C. At this temperature, Bi oxide is not reduced. Reduction at higher temperature leads to the formation of Pd—Bi intermetallic NPs. The exact structure depends on the composition. For Pd—Bi IMCs, there are three major IMCs that are possible in the phase diagram, Pd<sub>3</sub>Bi, PdBi, and PdBi<sub>2</sub>. In this study, the characterizations were consistent with the formation of the Pd<sub>3</sub>Bi phase or a Bi/Pd ratio of 0.33.

At low Bi loading, for example, in Pd-Bi/SiO<sub>2</sub>-0.12, there is insufficient Bi to form a full alloy. By EXAFS spectroscopy, the formation of an intermetallic NP is confirmed. From the STEM, DRIFTS, and catalytic results, it is observed that the alloy phase is present on the NP surface and the particle interior remains mostly metallic Pd. Core—shell morphologies are consistent with IMCs and not solid solution bimetallic NPs.<sup>26,53</sup> Although the PDH selectivity is improved compared to that of Pd NPs, the DRIFTS spectra show not only linear-bonded peak, typical of Pd<sub>3</sub>Bi surface regions, but also bridgebonded CO, typical of Pd ensembles, and suggests that a full surface alloy has not been achieved at this loading.

For Pd-Bi/SiO<sub>2</sub>-0.25, there is also not sufficient Bi to form a full Pd<sub>3</sub>Bi NP. EXAFS spectroscopy shows a higher level of Bi in the NPs, while STEM shows a Pd@Pd3Bi IMC core-shell structure (Figure 10B,F). The improved PDH selectivity and stability and improved acetylene semihydrogenation selectivity compared with Pd-Bi/SiO<sub>2</sub>-0.12 suggest the formation of the full Pd<sub>3</sub>Bi surface alloy. The DRIFTS spectra indicate that the surface Pd binds CO linearly, consistent with a monolayer coverage of the Pd<sub>3</sub>Bi IMC. The linear CO frequency at saturation coverage, however, is shifted to lower wavenumbers than for that of Pd. Such shifts are often interpreted as changes in electronic properties of the metal, resulting in the decreased metal-adsorbate bond energy. However, the XPS spectra suggest little change in the electronic properties in Pd and Pd<sub>3</sub>Bi IMCs. IR frequency shifts to lower wavenumbers, however, could also be interpreted as site isolation of adsorbed CO.<sup>39-44</sup> For example, for Pd NPs at lower coverages of CO, there is a decrease in the dipole-dipole interactions and shift to lower frequencies. The Pd-Pd bond distance in the Pd<sub>3</sub>Bi NPs determined by EXAFS spectroscopy is 2.80 Å, which is

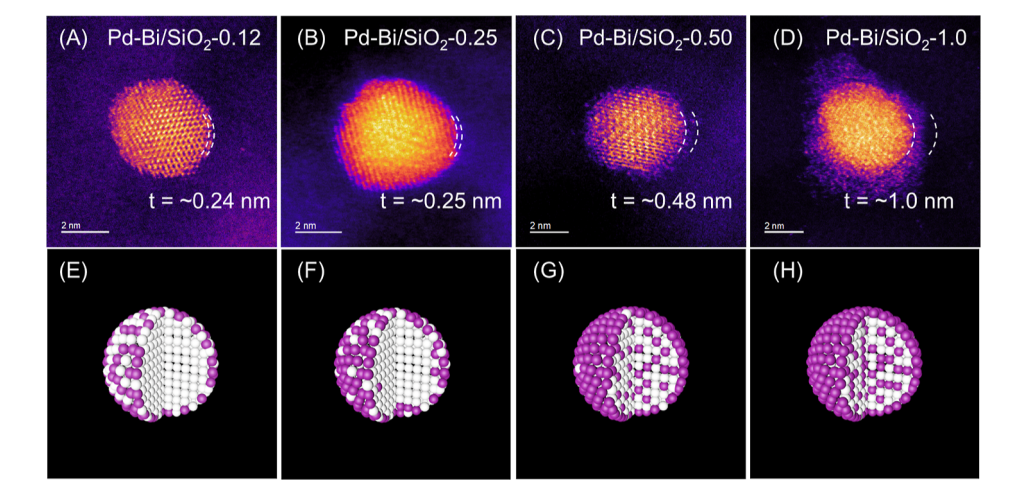
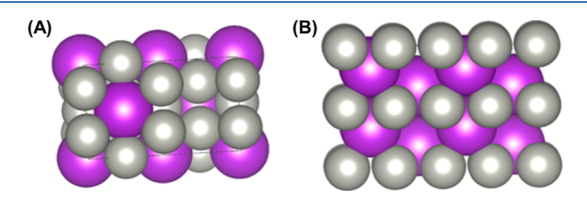


Figure 10. Structure evolution of Pd-Bi NPs along with the increase in Bi content. (A–D) HAADF images of Pd-Bi/SiO<sub>2</sub>-0.12 to Pd-Bi/SiO<sub>2</sub>-1.0 in fake color, and the corresponding thicknesses (t) of BiO<sub>x</sub> were marked along with Bi increasing; (E–H) schematics of the most possible atom structures under working conditions corresponding to HAADF images. Pd atoms are shown in white, and Bi atoms are shown in purple.

much longer than that in Pd NPs, that is, 2.73 Å. Thus, the lower frequency of the linear CO peaks for surfaces with Pd<sub>3</sub>Bi likely results from the weakened CO dipole-dipole interactions due to the increased Pd bond distance. These isolated Pd active sites efficiently suppress the hydrogenolysis rate in PDH and lead to the greatly enhanced propylene selectivity in PDH (95% at 25% propane conversion) compared to that of Pd NPs (44% at 25% propane conversion). In acetylene semihydrogenation, it has been reported that ethylene adsorbs much weaker on the isolated Pd active sites through the  $\pi$ -bonded adsorption mode,  $^{25,54-5}$ which prevents the ethylene from over hydrogenation to ethane and, therefore, promotes the desorption of ethylene as the desired product compared to Pd NPs. The improved selectivity for PDH and acetylene semihydrogenation is attributed to the isolated Pd sites in Pd-Bi alloy.

For Pd-Bi/SiO<sub>2</sub>-0.50, there is sufficient Bi to give a full Pd<sub>3</sub>Bi with some excess Bi in the catalyst. The EXAFS bond distances of Pd-Pd at 2.80 Å and Pd-Bi at 2.83 Å and Pd-Pd/Pd-Bi coordination ratios are consistent with small Pd<sub>3</sub>Bi NPs. The structure of Pd<sub>3</sub>Bi is shown in Figure 11A. Moreover,



**Figure 11.** (A) Structure of Pd<sub>3</sub>Bi, Pd–Pd = 2.87 Å, Pd–Bi = 2.88 Å, space group = *Pmma*,  $\alpha = 90^{\circ}$ ,  $\beta = 90^{\circ}$ , and  $\gamma = 90^{\circ}$ . (B) Structure of PdBi, Pd–Pd = 2.85 Å, Pd–Bi = 2.83 Å, space group =  $P6_3/mmc$ ,  $\alpha = 90^{\circ}$ ,  $\beta = 90^{\circ}$ , and  $\gamma = 120^{\circ}$ . Pd atoms are shown in gray, and Bi atoms are shown in purple.

STEM shows that the bimetallic particle is a single phase (Figure 10C,G). In addition, STEM (Figures 2C and 10C,D) shows that the excess Bi content is present as oxide covering the  $Pd_3Bi$  NPs. The partial coverage of the surface with a noncatalytic phase is consistent with the high PDH and acetylene semihydrogenation selectivity but lower rates for both reactions.

For Pd-Bi/SiO<sub>2</sub>-1.0, there is sufficient Bi to form a PdBi IMC, Figure 11B. If this structure were formed, there would be little additional Bi oxide and the catalyst would be expected to be highly selective and active since the Pd-Pd and Pd-Bi bond distances are very similar to those in Pd<sub>3</sub>Bi. While elemental map by EDX in Figure S5 shows that all of the Bi is localized near the bimetallic NP, Figure 10D shows that there is a thick Bi-rich layer that surrounds the inner Pd-Bi alloy core. The coverage of this Bi overlayer leads to a significant drop in the PDH and acetylene semihydrogenation rates, and the catalysts have a very low CO chemisorption capacity, suggesting few exposed Pd sites. Thus, while there is sufficient Bi to form the PdBi intermetallic alloy, it does not appear to form. Although the Pd-Pd and Pd-Bi bond distances in the Pd<sub>3</sub>Bi and PdBi phase are similar, their structures have very different symmetries. Therefore, to incorporate additional Bi atoms into Pd3Bi NPs, many atoms would need to simultaneously move lattice positions to give the PdBi structure. This structural rearrangement is apparently energetically too high to occur kinetically at the 550 °C reduction temperature.

While bimetallic catalysts often have improved catalytic performance, as this study shows, optimum performance is determined by more than just the formation of the alloy structure. If the oxide promoter, which is reduced to from the bimetallic NP, is sufficiently mobile during reduction or reaction conditions, the excess oxide may cover the alloy NP, leading to low rates. For many bimetallic Pd and Pt catalysts prepared via the IWI method, there is often a large amount of excess oxide and only a small portion of which undergoes reduction to form the alloy. For more readily reducible promoters, such as Sn, In, and Bi, promoter-rich compositions may result in irreversible loss in rate at high temperatures. 11,31,58 Recently, the colloidal synthesis of Pt-In IMCs where all the In atoms were present in the IMC alloy NP displayed high selectivity and stability at high reaction temperatures up to about 800 °C. <sup>59</sup> Thus, the thermal stability and excellent catalytic properties of intermetallic alloys can be maintained at very high reaction temperatures. However, for similar alloy compositions prepared by a traditional IWI synthesis, there was excess In<sub>2</sub>O<sub>3</sub> promoter in the catalyst. For the latter, at elevated temperature, the catalytic sites were covered by the promoter oxide, resulting in permanent loss of activity. Thus, the stability and mobility of the promoter oxide under the reaction conditions also play an important role in the effectiveness of alloy catalysts.

**4.2.** General Properties of an Effective Promoter for Intermetallic Alloy Formation. Many alloy compositions of group 8 metals have been synthesized and evaluated for different catalytic reactions. For many alloys, different compositions lead to differences in the catalytic performance. However, for many alloys, structural details, for example, surface coverage, particle morphology, atomic order, surface structures, and their effect on the catalytic performance, have not been determined. As shown in this study, in addition to the catalytically active NPs, the excess, noncatalytic promoter oxide can also have a strong influence on the performance.

In general, there are several properties that are required for an effective promotor. For example, bimetallic alloy catalysts are synthesized from metal compounds, for example, oxides, chlorides, organometallic compounds, and so forth. Thus, the first property of the promoter compound is that it needs to be reducible to the metallic state, which occurs during pretreatment or under reaction conditions. Many transition and main group promoter compounds, however, are often difficult to reduce in the absence of a catalytic metal. However, in the presence of a group 8 NP and spillover  $H_2$ , a bimetallic alloy is formed.

For structure-sensitive reactions, small ensemble and isolated catalytic sites give improved performance. P-11,15,20,21,23,26,31,32,60-62 If the melting point of the alloy NP is near that pre-treatment or reduction temperature, often a solid solution is formed. In order to obtain small catalytic ensembles and the highest catalytic selectivity, promoter-rich bimetallic compositions are required, often resulting in few surface-active sites and low rates due to the high dilution. However, if the promoter and group 8 metals have different atomic radii or different monometallic structures and symmetry, IMCs may be formed. The possible IMCs for any two metals can be determined from the phase diagrams. Since catalytic alloys are formed kinetically, that is, by reduction of the metal salts, rather than thermodynamically, for example, slow cooling of a binary metallic liquid, not all IMCs are formed. The group 8 metal is first reduced. This

kinetic formation of the IMCs begins by surface enrichment of the group 8 metal with the promoter atom. As a result, the binary alloy often forms an intermetallic structure with the same or very similar symmetry as that of the group 8 metal. By forming IMCs with a similar structure, only a few surface atoms need to move to incorporate the second metal atom. For bimetallic catalysts where there is no bulk cubic phase, surface cubic structures may also be formed. These, however, exist only as surface IMCs, although these do significantly improve the catalytic performance.

With increasing loadings of promoter metal, a full layer of the surface IMC is formed. These core—intermetallic shell catalysts require less promoter atoms for optimal selectivity compared to solid solution alloy of the same composition. Since intermetallic alloys also have the fixed stoichiometric structures, the number of catalytic sites is higher than that in solid solutions with the same selectivity. At higher levels of promoter, a multilayer alloy with a smaller monometallic core is formed, ultimately resulting in full alloy formation. <sup>10,11,60–62</sup>

The initial intermetallic alloy can also incorporate additional metallic promoter atoms to form a more promoter-rich alloy if the symmetry of the second intermetallic phase is similar to that of the first IMC.  $^{11}$  As with the  $Pd_3Bi$  IMC, where the symmetry of the PdBi phase is significantly different, the excess promoter will not form a new intermetallic phase, and the excess Bi oxide will be present on the support. If the oxide is mobile under the reaction conditions, it can cover the active site, resulting in low permanent loss in activity.

Finally, for high-temperature reactions, phase stability and sintering resistance are essential for long-term performance. The melting point of each intermetallic structure is also given in the binary phase diagrams. These melting points, however, are for bulk structures, and NPs have significantly lower melting points compared to bulk alloys. Thus, for sintering resistance, one should select a promoter metal, which forms an IMC with the melting point well above the reaction temperature. If the reaction temperature is near the melting point, the IMC may convert to a solid solution and have lower selectivity. For example, the intermetallic  $Pd_3Cu$  prepared at low temperature by colloidal synthesis was observed to form a solid solution after reduction at 375 °C.  $^{56}$ 

As this study shows, alloy catalysts lead to improved selectivity, rates, and stability. However, optimization of the performance requires more than the formation of the bimetallic NPs. There are several other properties of promoters such as the radius of the reduced metal atom, the IMC symmetry, and mobility of the excess promoter oxide that can also control the extent of surface alloy coverage, type of alloy structure, and even the presence of oxide overlayers on the active NP surface and can significantly influence the catalytic performance. With modern characterization tools, the structure of alloy NPs, catalytic surface, and the other noncatalytic phases can be determined. As demonstrated in this study, the catalyst performance not only is determined by the alloy structure but also can be significantly affected by the properties of the noncatalytic promoter.

## 5. CONCLUSIONS

A series of Pd—Bi bimetallic catalysts with different Bi levels has been synthesized using the IWI method. The combined characterizations of *in situ* XAS, HAADF imaging, *in situ* XPS, EDS, and DRIFTS led to the atomic-level understanding of the structural evolution of bimetallic catalysts as the Bi loading

increases. At low Bi loading, the Pd surface is partially covered with a  $Pd_3Bi$  alloy on a Pd core NP. At slightly higher Bi loading, the surface is a monolayer of  $Pd_3Bi$  on Pd, that is,  $Pd@Pd_3Bi$ . At high Bi loadings, there is a full  $Pd_3Bi$  alloy NP with the excess Bi-rich layer partially covering the active surface, leading to lower activity.

The selectivity, activity, and stability were found to significantly depend on the NP surface composition. In  $Pd_3Bi$  IMCs, there are threefold Pd sites; however, an adjacent Pd–Pd distance of 2.80 Å occurs at a longer, nonbonding distance than that in Pd NPs. The DRIFTS spectrum indicates that the adjacent Pd distance is too long to bridge-bond CO. These, spatially isolated Pd sites give rise to the superior selectivity in PDH (95%) and acetylene semihydrogenation (80%). At high Bi loading (Bi/Pd = 0.5–1.0), a more Bi-rich PdBi intermetallic alloy is not formed, and the excess Bi promoter covers the  $Pd_3Bi$  alloy, leading to low activity. Such structural details lead to a more fundamental understanding of the structure–performance relationship.

#### ASSOCIATED CONTENT

## **Supporting Information**

The Supporting Information is available free of charge at https://pubs.acs.org/doi/10.1021/acscatal.2c00642.

STEM images and corresponding particle size of 2% Pd/SiO<sub>2</sub>; Pd 3d *in situ* XPS spectra of Pd NPs and Pd-Bi catalysts; propylene selectivity over reaction time of Pd NPs and Pd-Bi catalysts; acetylene conversion as a function of temperature for 1 wt % Pd/Al<sub>2</sub>O; and elemental composition analysis of Pd-Bi/SiO<sub>2</sub>-1.0 (PDF)

## AUTHOR INFORMATION

## **Corresponding Authors**

Guanghui Zhang — State Key Laboratory of Fine Chemicals, School of Chemical Engineering, Dalian University of Technology, Dalian 116024, China; orcid.org/0000-0002-5854-6909; Email: gzhang@dlut.edu.cn

Wei Liu – Division of Energy Research Resources, Dalian National Laboratory for Clean Energy, Dalian Institute of Chemical Physics, Chinese Academy of Sciences, Dalian 116023, China; orcid.org/0000-0002-4403-737X; Email: weiliu@dicp.ac.cn

Jeffrey T. Miller − Davidson School of Chemical Engineering, Purdue University, West Lafayette, Indiana 47907, United States; orcid.org/0000-0002-6269-0620; Email: mill1194@purdue.edu

#### Authors

Wenqing Zhang — Davidson School of Chemical Engineering, Purdue University, West Lafayette, Indiana 47907, United States

Xiaoben Zhang — Division of Energy Research Resources, Dalian National Laboratory for Clean Energy, Dalian Institute of Chemical Physics, Chinese Academy of Sciences, Dalian 116023, China; University of Chinese Academy of Sciences, Beijing 100049, China; orcid.org/0000-0001-5033-2642

Jianyang Wang — State Key Laboratory of Fine Chemicals, School of Chemical Engineering, Dalian University of Technology, Dalian 116024, China

- Arnab Ghosh Department of Chemical & Biological Engineering & Center for Micro-engineered Materials, University of New Mexico, Albuquerque, New Mexico 87131, United States
- Jie Zhu State Key Laboratory of Fine Chemicals, School of Chemical Engineering, Dalian University of Technology, Dalian 116024, China; orcid.org/0000-0003-0651-8022
- Nicole J. LiBretto Davidson School of Chemical Engineering, Purdue University, West Lafayette, Indiana 47907, United States
- Abhaya K. Datye Department of Chemical & Biological Engineering & Center for Micro-engineered Materials, University of New Mexico, Albuquerque, New Mexico 87131, United States; orcid.org/0000-0002-7126-8659

Complete contact information is available at: https://pubs.acs.org/10.1021/acscatal.2c00642

#### **Author Contributions**

\*W.Z. and X.Z. contributed equally.

#### Notes

The authors declare no competing financial interest.

## ACKNOWLEDGMENTS

W.Z., N.J.L., A.K.D., and J.T.M. were supported in part by the National Science Foundation under Cooperative Agreement no. EEC-1647722. G.Z. would like to acknowledge the National Natural Science Foundation of China (21902019) and the Liaoning Revitalization Talents Program (XLYC2008032). W.L. acknowledges the National Natural Science Foundation of China (22072150). Use of the Center for Nanoscale Materials and Advanced Photon Source, both Office of Science user facilities, was supported by the U.S. Department of Energy, Office of Science, Office of Basic Energy Sciences, under contract no. DE-AC02-06CH11357. MRCAT operations and the beamline 10-BM were supported by the Department of Energy and the MRCAT member institutions.

#### REFERENCES

- (1) Mitchell, S.; Qin, R.; Zheng, N.; Pérez-Ramírez, J. Nanoscale engineering of catalytic materials for sustainable technologies. *Nat. Nanotech.* **2021**, *16*, 129–139.
- (2) Chen, G.; Xu, C.; Huang, X.; Ye, J.; Gu, L.; Li, G.; Tang, Z.; Wu, B.; Yang, H.; Zhao, Z.; Zhou, Z.; Fu, G.; Zheng, N. Interfacial electronic effects control the reaction selectivity of platinum catalysts. *Nat. Mater.* **2016**, *15*, 564–569.
- (3) Marshall, S. T.; O'Brien, M.; Oetter, B.; Corpuz, A.; Richards, R. M.; Schwartz, D. K.; Medlin, J. W. Controlled selectivity for palladium catalysts using self-assembled monolayers. *Nat. Mater.* **2010**, *9*, 853–
- (4) Lee, I.; Delbecq, F.; Morales, R.; Albiter, M. A.; Zaera, F. Tuning selectivity in catalysis by controlling particle shape. *Nat. Mater.* **2009**, *8*, 132–138.
- (5) Somorjai, G. A.; Park, J. Y. Molecular factors of catalytic selectivity. *Angew. Chem., Int. Ed.* **2008**, 47, 9212–9228.
- (6) Nørskov, J. K.; Bligaard, T.; Hvolbæk, B.; Abild-Pedersen, F.; Chorkendorff, I.; Christensen, C. H. The nature of the active site in heterogeneous metal catalysis. *Chem. Soc. Rev.* **2008**, *37*, 2163–2171.
- (7) Ye, C.; Peng, M.; Wang, Y.; Zhang, N.; Wang, D.; Jiao, M.; Miller, J. T. Surface Hexagonal Pt1Sn1 Intermetallic on Pt Nanoparticles for Selective Propane Dehydrogenation. ACS Appl. Mater. Interface 2020, 12, 25903–25909.
- (8) Zhang, G.; Ye, C.; Liu, W.; Zhang, X.; Su, D.; Yang, X.; Chen, J. Z.; Wu, Z.; Miller, J. T. Diffusion-Limited Formation of Non-

- equilibrium Intermetallic Nanophase for Selective Dehydrogenation. *Nano Lett.* **2019**, *19*, 4380–4383.
- (9) Yang, C.; Wu, Z.; Zhang, G.; Sheng, H.; Tian, J.; Duan, Z.; Sohn, H.; Kropf, A. J.; Wu, T.; Krause, T. R.; Miller, J. T. Promotion of Pd nanoparticles by Fe and formation of a Pd3Fe intermetallic alloy for propane dehydrogenation. *Catal. Today* **2019**, 323, 123–128.
- (10) LiBretto, N. J.; Yang, C.; Ren, Y.; Zhang, G.; Miller, J. T. Identification of Surface Structures in Pt3Cr Intermetallic Nanocatalysts. *Chem. Mater.* **2019**, *31*, 1597–1609.
- (11) Cesar, L. G.; Yang, C.; Lu, Z.; Ren, Y.; Zhang, G.; Miller, J. T. Identification of a Pt3Co Surface Intermetallic Alloy in Pt-Co Propane Dehydrogenation Catalysts. ACS Catal. 2019, 9, 5231-5244.
- (12) He, Y.; Liang, L.; Liu, Y.; Feng, J.; Ma, C.; Li, D. Partial hydrogenation of acetylene using highly stable dispersed bimetallic Pd–Ga/MgO–Al2O3 catalyst. *J. Catal.* **2014**, *309*, 166–173.
- (13) Armbrüster, M.; Kovnir, K.; Friedrich, M.; Teschner, D.; Wowsnick, G.; Hahne, M.; Gille, P.; Szentmiklósi, L.; Feuerbacher, M.; Heggen, M.; Rosenthal, D.; Schlögl, R.; Grin, Y. Al13Fe4 as a low-cost alternative for palladium in heterogeneous hydrogenation. *Nat. Mater.* **2012**, *11*, 690–693.
- (14) Liu, Y.; Liu, X.; Feng, Q.; He, D.; Zhang, L.; Lian, C.; Shen, R.; Zhao, G.; Ji, Y.; Wang, D.; Zhou, G.; Li, Y. Intermetallic NixMy (M=Ga and Sn) Nanocrystals: A Non-precious Metal Catalyst for Semi-Hydrogenation of Alkynes. *Adv. Mater.* **2016**, *28*, 4747–4754.
- (15) Zhou, H.; Yang, X.; Li, L.; Liu, X.; Huang, Y.; Pan, X.; Wang, A.; Li, J.; Zhang, T. PdZn Intermetallic Nanostructure with Pd–Zn–Pd Ensembles for Highly Active and Chemoselective Semi-Hydrogenation of Acetylene. *ACS Catal.* **2016**, *6*, 1054–1061.
- (16) Pei, G. X.; Liu, X. Y.; Wang, A.; Lee, A. F.; Isaacs, M. A.; Li, L.; Pan, X.; Yang, X.; Wang, X.; Tai, Z.; Wilson, K.; Zhang, T. Ag Alloyed Pd Single-Atom Catalysts for Efficient Selective Hydrogenation of Acetylene to Ethylene in Excess Ethylene. ACS Catal. 2015, 5, 3717—3725.
- (17) Mei, D.; Neurock, M.; Smith, C. M. Hydrogenation of acetylene-ethylene mixtures over Pd and Pd-Ag alloys: First-principles-based kinetic Monte Carlo simulations. *J. Catal.* **2009**, 268, 181–195.
- (18) Yang, B.; Burch, R.; Hardacre, C.; Headdock, G.; Hu, P. Influence of surface structures, subsurface carbon and hydrogen, and surface alloying on the activity and selectivity of acetylene hydrogenation on Pd surfaces: A density functional theory study. *J. Catal.* **2013**, 305, 264–276.
- (19) Studt, F.; Abild-Pedersen, F.; Bligaard, T.; Sørensen, R. Z.; Christensen, C. H.; Nørskov, J. K. Identification of non-precious metal alloy catalysts for selective hydrogenation of acetylene. *Science* **2008**, 320, 1320–1322.
- (20) Purdy, S. C.; Seemakurthi, R. R.; Mitchell, G. M.; Davidson, M.; Lauderback, B. A.; Deshpande, S.; Wu, Z.; Wegener, E. C.; Greeley, J.; Miller, J. T. Structural trends in the dehydrogenation selectivity of palladium alloys. *Chem. Sci.* **2020**, *11*, 5066–5081.
- (21) Childers, D. J.; Schweitzer, N. M.; Shahari, S. M. K.; Rioux, R. M.; Miller, J. T.; Meyer, R. J. Modifying structure-sensitive reactions by addition of Zn to Pd. *J. Catal.* **2014**, *318*, 75–84.
- (22) Pei, G. X.; Liu, X. Y.; Yang, X.; Zhang, L.; Wang, A.; Li, L.; Wang, H.; Wang, X.; Zhang, T. Performance of Cu-Alloyed Pd Single-Atom Catalyst for Semihydrogenation of Acetylene under Simulated Front-End Conditions. *ACS Catal.* **2017**, *7*, 1491–1500.
- (23) Feng, Q.; Zhao, S.; Wang, Y.; Dong, J.; Chen, W.; He, D.; Wang, D.; Yang, J.; Zhu, Y.; Zhu, H.; Gu, L.; Li, Z.; Liu, Y.; Yu, R.; Li, J.; Li, Y. Isolated single-atom Pd sites in intermetallic nanostructures: high catalytic selectivity for semihydrogenation of alkynes. *J. Am. Chem. Soc.* **2017**, 139, 7294–7301.
- (24) Pei, G. X.; Liu, X. Y.; Wang, A.; Li, L.; Huang, Y.; Zhang, T.; Lee, J. W.; Jang, B. W. L.; Mou, C.-Y. Promotional effect of Pd single atoms on Au nanoparticles supported on silica for the selective hydrogenation of acetylene in excess ethylene. *New J. Chem.* **2014**, 38, 2043–2051.
- (25) Liu, F.; Xia, Y.; Xu, W.; Cao, L.; Guan, Q.; Gu, Q.; Yang, B.; Lu, J. Integration of Bimetallic Electronic Synergy with Oxide Site

- Isolation Improves the Selective Hydrogenation of Acetylene. *Angew. Chem., Int. Ed.* **2021**, *60*, 19324–19330.
- (26) Ma, Z.; Wu, Z.; Miller, J. T. Effect of Cu content on the bimetallic Pt-Cu catalysts for propane dehydrogenation. *Catal., Struct. React.* **2017**, *3*, 43–53.
- (27) Xie, C.; Niu, Z.; Kim, D.; Li, M.; Yang, P. Surface and interface control in nanoparticle catalysis. *Chem. Rev.* **2019**, *120*, 1184–1249.
- (28) Rehr, J. J.; Booth, C. H.; Bridges, F.; Zabinsky, S. I. X-ray-absorption fine structure in embedded atoms. *Phys. Rev. B: Condens. Matter Mater. Phys.* **1994**, 49, 12347–12350.
- (29) Ressler, T. WinXAS: a Program for X-ray Absorption Spectroscopy Data Analysis under MS-Windows. *J. Synchrotron Radiat.* **1998**, *5*, 118–122.
- (30) Zhou, M.; Guo, J.; Zhao, B.; Li, C.; Zhang, L.; Fang, J. Improvement of Oxygen Reduction Performance in Alkaline Media by Tuning Phase Structure of Pd—Bi Nanocatalysts. *J. Am. Chem. Soc.* **2021**, *143*, 15891.
- (31) Wu, Z.; Wegener, E. C.; Tseng, H.-T.; Gallagher, J. R.; Harris, J. W.; Diaz, R. E.; Ren, Y.; Ribeiro, F. H.; Miller, J. T. Pd-In intermetallic alloy nanoparticles: highly selective ethane dehydrogenation catalysts. *Catal. Sci. Technol.* **2016**, *6*, 6965–6976.
- (32) Mitsudome, T.; Mikami, Y.; Matoba, M.; Mizugaki, T.; Jitsukawa, K.; Kaneda, K. Design of a Silver-Cerium Dioxide Core-Shell Nanocomposite Catalyst for Chemoselective Reduction Reactions. *Angew. Chem., Int. Ed.* **2012**, *51*, 136–139.
- (33) Miller, J. T.; Kropf, A. J.; Zha, Y.; Regalbuto, J. R.; Delannoy, L.; Louis, C.; Bus, E.; van Bokhoven, J. A. The effect of gold particle size on AuAu bond length and reactivity toward oxygen in supported catalysts. *J. Catal.* **2006**, 240, 222–234.
- (34) Lear, T.; Marshall, R.; Antonio Lopez-Sanchez, J. A.; Jackson, S. D.; Klapötke, T. M.; Bäumer, M.; Rupprechter, G.; Freund, H. J.; Lennon, D. The application of infrared spectroscopy to probe the surface morphology of alumina-supported palladium catalysts. *J. Chem. Phys.* **2005**, *123*, 174706.
- (35) Lu, J.; Fu, B.; Kung, M. C.; Xiao, G.; Elam, J. W.; Kung, H. H.; Stair, P. C. Coking- and Sintering-Resistant Palladium Catalysts Achieved Through Atomic Layer Deposition. *Science* **2012**, 335, 1205–1208.
- (36) Onda, A.; Komatsu, T.; Yashima, T. Characterizations and catalytic properties of fine particles of Ni–Sn intermetallic compounds supported on SiO2. *J. Catal.* **2004**, 221, 378–385.
- (37) Komatsu, T.; Kishi, T.; Gorai, T. Preparation and catalytic properties of uniform particles of Ni3Ge intermetallic compound formed inside the mesopores of MCM-41. *J. Catal.* **2008**, 259, 174–182.
- (38) Komatsu, T.; Ikenaga, H. Dehydroisomerization of butane into isobutene on Pt—Sn intermetallic compounds supported on H-SAPO-11. *J. Catal.* **2006**, *241*, 426–434.
- (39) Primet, M. Electronic transfer and ligand effects in the infrared spectra of adsorbed carbon monoxide. *J. Catal.* **1984**, 88, 273–282.
- (40) Bartók, M.; Sárkány, J.; Sitkei, A. Investigation of interactions between metals and adsorbed organic compounds by infrared spectroscopic study of adsorbed CO: I. Infrared study of CO adsorption and desorption on Pt/Cab-O-Sil catalyst. *J. Catal.* 1981, 72, 236–245.
- (41) Crossley, A.; King, D. A. Infrared spectra for co isotopes chemisorbed on Pt "111": Evidence for strong absorbate coupling interactions. *Surf. Sci.* **1977**, *68*, 528–538.
- (42) Hendrickx, H. A. C. M.; des Bouvrie, C.; Ponec, V. On the electronic competition effect upon CO adsorption on metals. *J. Catal.* **1988**, *109*, 120–125.
- (43) Sárkány, J.; Bartók, M.; Gonzalez, R. D. The modification of CO adlayers on PtSiO2 catalysts by preadsorbed oxygen: An infrared and pulse microreactor study. *J. Catal.* **1983**, *81*, 347–357.
- (44) Stoop, F.; Toolenaar, F.; Ponec, V. Geometric and ligand effects in the infrared spectra of adsorbed carbon monoxide. *J. Catal.* **1982**, 73, 50–56.
- (45) He, Y.; Fan, J.; Feng, J.; Luo, C.; Yang, P.; Li, D. Pd nanoparticles on hydrotalcite as an efficient catalyst for partial

- hydrogenation of acetylene: Effect of support acidic and basic properties. *J. Catal.* **2015**, 331, 118–127.
- (46) Chen, Z.; He, Y.-C.; Chen, J.-H.; Fu, X.-Z.; Sun, R.; Chen, Y.-X.; Wong, C.-P. PdCu Alloy Flower-like Nanocages with High Electrocatalytic Performance for Methanol Oxidation. *J. Phys. Chem. C* 2018, 122, 8976–8983.
- (47) Hong, L.; Dong, Q.; Qin, Q.; Li, H.; Xie, J.; Yu, G.; Chen, H. PdBi alloy nanoparticle-enhanced catalytic activity toward formic acid oxidation. *Int. J. Hydrogen Energy* **2019**, *44*, 19900–19907.
- (48) Fung, S. C. XPS studies of strong metal-support interactions (SMSI)-Pt/TiO/sub 2. *J. Catal.* **1982**, *76*, 225. , Medium: X; Size: Pages: 225-230 2009-12-17
- (49) Yan, H.; Liu, Y.; Zhang, T.; Jin, Z.; Wang, M.; Xie, Y. P.; Guo, H. Greatly changed performance of a metal Pd catalyst by a rather easily formed and removed species—PdH x. *Catal. Sci. Technol.* **2018**, 8, 3238—3245.
- (50) Lou, B.; Kang, H.; Yuan, W.; Ma, L.; Huang, W.; Wang, Y.; Jiang, Z.; Du, Y.; Zou, S.; Fan, J. Highly Selective Acetylene Semihydrogenation Catalyst with an Operation Window Exceeding 150° C. ACS Catal. 2021, 11, 6073–6080.
- (51) Vilé, G.; Albani, D.; Nachtegaal, M.; Chen, Z.; Dontsova, D.; Antonietti, M.; López, N.; Pérez-Ramírez, J. A stable single-site palladium catalyst for hydrogenations. *Angew. Chem., Int. Ed.* **2015**, 54, 11265–11269.
- (52) Benavidez, A. D.; Burton, P. D.; Nogales, J. L.; Jenkins, A. R.; Ivanov, S. A.; Miller, J. T.; Karim, A. M.; Datye, A. K. Improved selectivity of carbon-supported palladium catalysts for the hydrogenation of acetylene in excess ethylene. *Appl. Catal., A* **2014**, *482*, 108–115.
- (53) Wang, C.; Hu, F.; Yang, H.; Zhang, Y.; Lu, H.; Wang, Q. 1.82 wt.% Pt/N, P co-doped carbon overwhelms 20 wt.% Pt/C as a high-efficiency electrocatalyst for hydrogen evolution reaction. *Nano Res.* 2017, 10, 238–246.
- (54) Kuo, C.-T.; Lu, Y.; Kovarik, L.; Engelhard, M.; Karim, A. M. Structure Sensitivity of Acetylene Semi-Hydrogenation on Pt Single Atoms and Subnanometer Clusters. *ACS Catal.* **2019**, *9*, 11030–11041.
- (55) Zou, S.; Lou, B.; Yang, K.; Yuan, W.; Zhu, C.; Zhu, Y.; Du, Y.; Lu, L.; Liu, J.; Huang, W.; Yang, B.; Gong, Z.; Cui, Y.; Wang, Y.; Ma, L.; Ma, J.; Jiang, Z.; Xiao, L.; Fan, J. Grafting nanometer metal/oxide interface towards enhanced low-temperature acetylene semi-hydrogenation. *Nat. Commun.* **2021**, *12*, 5770.
- (56) Huang, F.; Deng, Y.; Chen, Y.; Cai, X.; Peng, M.; Jia, Z.; Xie, J.; Xiao, D.; Wen, X.; Wang, N.; Jiang, Z.; Liu, H.; Ma, D. Anchoring Cu1 species over nanodiamond-graphene for semi-hydrogenation of acetylene. *Nat. Commun.* **2019**, *10*, 4431.
- (57) Huang, F.; Deng, Y.; Chen, Y.; Cai, X.; Peng, M.; Jia, Z.; Ren, P.; Xiao, D.; Wen, X.; Wang, N.; Liu, H.; Ma, D. Atomically Dispersed Pd on Nanodiamond/Graphene Hybrid for Selective Hydrogenation of Acetylene. *J. Am. Chem. Soc.* **2018**, *140*, 13142–13146.
- (58) Siri, G. J.; Ramallo-López, J. M.; Casella, M. L.; Fierro, J. L. G.; Requejo, F. G.; Ferretti, O. A. XPS and EXAFS study of supported PtSn catalysts obtained by surface organometallic chemistry on metals. *Appl. Catal., A* **2005**, 278, 239–249.
- (59) Escorcia, N. J.; LiBretto, N. J.; Miller, J. T.; Li, C. W. Colloidal Synthesis of Well-Defined Bimetallic Nanoparticles for Nonoxidative Alkane Dehydrogenation. *ACS Catal.* **2020**, *10*, 9813–9823.
- (60) Wu, Z.; Bukowski, B. C.; Li, Z.; Milligan, C.; Zhou, L.; Ma, T.; Wu, Y.; Ren, Y.; Ribeiro, F. H.; Delgass, W. N.; Greeley, J.; Zhang, G.; Miller, J. T. Changes in Catalytic and Adsorptive Properties of 2 nm Pt3Mn Nanoparticles by Subsurface Atoms. *J. Am. Chem. Soc.* **2018**, 140, 14870–14877.
- (61) Wegener, E. C.; Wu, Z.; Tseng, H.-T.; Gallagher, J. R.; Ren, Y.; Diaz, R. E.; Ribeiro, F. H.; Miller, J. T. Structure and reactivity of Pt-In intermetallic alloy nanoparticles: Highly selective catalysts for ethane dehydrogenation. *Catal. Today* **2018**, *299*, 146–153.
- (62) Cybulskis, V. J.; Bukowski, B. C.; Tseng, H.-T.; Gallagher, J. R.; Wu, Z.; Wegener, E.; Kropf, A. J.; Ravel, B.; Ribeiro, F. H.; Greeley, J.; Miller, J. T. Zinc Promotion of Platinum for Catalytic Light Alkane

**ACS Catalysis** pubs.acs.org/acscatalysis

Dehydrogenation: Insights into Geometric and Electronic Effects. ACS Catal. 2017, 7, 4173-4181.

## **Recommended by ACS**

## **Achieving Ultra-High Selectivity to Hydrogen Production** from Formic Acid on Pd-Ag Alloys

Mustafa Karatok, Robert J. Madix, et al.

FEBRUARY 27, 2023

JOURNAL OF THE AMERICAN CHEMICAL SOCIETY

READ

## Highly Selective Activation of C-H Bond and Inhibition of C-C Bond Cleavage by Tuning Strong Oxidative Pd Sites

Meng Guo, Jiguang Deng, et al.

MAY 16, 2023

JOURNAL OF THE AMERICAN CHEMICAL SOCIETY

READ 🗹

## **Enhanced Hydrogenation Properties of Pd Single Atom** Catalysts with Atomically Dispersed Ba Sites as Electronic **Promoters**

Ying Zhang, Hongbing Ji, et al.

NOVEMBER 28, 2022

ACS CATALYSIS

READ 🗹

## Single-Atom Ni-Modified Al<sub>2</sub>O<sub>3</sub>-Supported Pd for Mild-Temperature Semi-hydrogenation of Alkynes

Xin Song, Jianguo Wang, et al.

NOVEMBER 22, 2022

ACS CATALYSIS

READ 🗹

Get More Suggestions >